

The White Dwarf Cooling Sequence of NGC 6397¹

Brad M. S. Hansen^{2,3}, Jay Anderson⁴, James Brewer⁵, Aaron Dotter⁶, Greg. G. Fahlman^{5,7}, Jarrod Hurley⁸, Jason Kalirai⁹, Ivan King¹⁰, David Reitzel², Harvey B. Richer⁵, R. Michael Rich², Michael M. Shara¹¹, Peter B. Stetson¹²

ABSTRACT

We present the results of a deep Hubble Space Telescope (HST) exposure of the nearby globular cluster NGC 6397, focussing attention on the cluster's white dwarf cooling sequence. This sequence is shown to extend over 5 magnitudes in depth, with an apparent cutoff at magnitude $F814W \sim 27.6$. We demonstrate, using both artificial star tests and the detectability of background galaxies at fainter magnitudes, that the cutoff is real and represents the truncation of the white dwarf luminosity function in this cluster. We perform a detailed comparison between cooling models and the observed distribution of white dwarfs in colour and magnitude, taking into account uncertainties in distance, extinction, white dwarf mass, progenitor lifetimes, binarity and cooling model uncertainties. After marginalising over these variables, we obtain values for the cluster distance modulus and age of $\mu_0 = 12.02 \pm 0.06$ and $T_c = 11.47 \pm 0.47$ Gyr (95% confidence limits). Our inferred distance and white dwarf initial-final mass relations are in good agreement with other independent determinations, and the cluster age is consistent with, but more precise than, prior determinations made using the main sequence turnoff method. In particular, within the context of the currently accepted Λ CDM cosmological model, this age places

¹Based on observations with the NASA/ESA Hubble Space Telescope, obtained at the Space Telescope Science Institute, which is operated by the Association of Universities for Research in Astronomy, Inc., under NASA contract NAS 5-26555. These observations are associated with proposal GO-10424

²Department of Astronomy, University of California Los Angeles, Los Angeles, CA 90095, hansen@astro.ucla.edu, reitzel@astro.ucla.edu, rmr@astro.ucla.edu

³Institute for Geophysics and Planetary Physics, University of California Los Angeles, Los Angeles, CA 90095

⁴Department of Physics and Astronomy, Rice University, Houston, TX 77005, jay@eeeyore.rice.edu

⁵Department of Physics & Astronomy, 6224 Agricultural Road, University of British Columbia, Vancouver, BC, V6T 1Z4, Canada, richer@astro.ubc.ca

⁶Department of Physics & Astronomy, Dartmouth College, 6127 Wilder Laboratory, Hanover, NH, aaron.l.dotter@dartmouth.edu

⁷Canada-France-Hawaii Telescope Corporation, P.O. Box 1597, Kamuela, HI, 96743, fahlman@cfht.hawaii.edu

⁸Department of Mathematics and Statistics, Monash University, Clayton, Victoria 3800, Australia, jarrod.hurley@sci.monash.edu.au

⁹Hubble Fellow, Lick Observatory, University of California Santa Cruz, Santa Cruz, CA, 95064, jkalirai@ucolick.org

¹⁰Department of Astronomy, University of Washington, Seattle, WA 98195, king@astro.washington.edu

¹¹Department of Astrophysics, Division of Physical Sciences, American Museum of Natural History, Central Park West at 79th St, New York, NY, 10024-5192, mshara@amnh.org

¹²Hertzberg Institute of Astrophysics, National Research Council, Victoria, BC, Canada, peter.stetson@nrc-cnrc.gc.ca

the formation of NGC 6397 at a redshift $z \sim 3$, at a time when the cosmological star formation rate was approaching its peak.

Subject headings: globular clusters: individual (NGC 6397), age – stars: white dwarfs, luminosity function, Population II – Galaxy: halo

1. Introduction

The oldest known stellar systems in the Milky Way are the globular clusters. As such, their nature reflects the conditions under which our Galaxy first formed and offers a unique window into the high redshift universe. Age determination of globular clusters by fitting models to the main sequence turnoff has a long and venerable history (Sandage 1953; Janes & Demarque 1983; Fahlman, Richer & VandenBerg 1985; Chieffi & Straniero 1989; VandenBerg, Bolte & Stetson 1996 and references therein). For a long period of time, the results of these studies led to a so-called ‘cosmological crisis’, in which the estimated cluster ages ($\sim 16 - 20$ Gyr) were larger than the age of the universe based on a variety of cosmological tests (e.g. Bolte & Hogan 1995). However, over the last decade, improvements in the distance measurements to globular clusters, particularly using the Hipparcos satellite, have resulted in a lower estimate for the mean age of the metal poor (hence oldest) globular clusters (> 10.4 Gyr at 95% confidence; Krauss & Chaboyer 2003), which is now consistent with the age of the universe estimated from microwave background measurements (Spergel et al 2003). As befits a mature method, the accuracy of this MSTO method is currently limited by a variety of systematic errors (distance and metallicity uncertainties, atmosphere models that don’t fit the shape of the turnoff). This method has been carried as far as it can go with current technology and further significant improvements must await technical advances, such as improvements in distance measurement using the Space Interferometry Mission (Chaboyer et al 2002).

In the past several years, we have embarked on a program to measure the ages of globular clusters by an entirely different method – measuring the white dwarf cooling sequence (WDCS) and determining the age by modeling the rate at which they cool (Hansen et al 2002; 2004). This method also has a distinguished history when applied to the stellar population in the solar neighbourhood (Winget et al 1987; Wood 1992; Hernanz et al 1994; Oswalt et al 1996; Leggett et al. 1998; Hansen 1999; Harris et al 2006) but it has only recently become possible to apply the same method to globular clusters because of the extreme requirements such measurements place on both resolution and photometric depth.

Our initial measurements of the age of Messier 4 (M4), the closest globular cluster to the sun, yielded a best-fit age of 12.1 Gyr, with a 95% lower bound of 10.3 Gyr. This is similar to the accuracy achieved by the latest MSTO analysis ($12.6^{+3.4}_{-2.2}$ Gyr) by Krauss & Chaboyer (2003). The M4 measurement was performed using the WFPC2 camera on the Hubble Space Telescope, which has since been superseded by the Advanced Camera for Surveys (ACS). The larger field and better resolution of ACS thus offers the possibility of improving on this result. Furthermore, the original M4 result was considered controversial by some (de Marchi et al. 2004), although unreasonably so in our opinion (Richer et al 2004; Hansen et al 2004). Nevertheless, an opportunity to repeat the experiment would serve to dispel any lingering doubts.

Consequently, we have observed a field in the second closest globular cluster to the sun, NGC 6397, using ACS on HST, with the goal of measuring the white dwarf cooling sequence to unprecedented depth and precision. In addition, the lower reddening (relative to M4) of this cluster and the inclusion of a series of short exposures (to avoid saturation of bright stars), allows us to perform a fit to the MSTO (Richer et al. 2007) simultaneously while fitting the WDCS – a measurement never before possible. In § 2, we describe

the observations and the reduction process, including characterisation and removal of background galaxies as well as the characterisation of our observational biases, using extensive artificial star tests. In § 3, we describe our modeling procedure and construct simulated cooling sequences which we then compare to the data. In § 4 we summarise our result and its implications.

2. Observations

The observational data consist of a series of images taken with ACS of a single field in NGC 6397, over the course of 126 orbits (4.7 days). The field is located 5 arcminutes southeast of the cluster core, overlapping that of several previous data sets taken by the Wide Field Planetary Camera 2 (WFPC2) in 1994 & 1997. All told the data set consists of 252 exposures (totalling 179.7 ksec) in the F814W filter and 126 exposures totalling 93.4 ksec in F606W. The F814W exposures were taken at the beginning and end of each visibility period, so that the F606W exposures were taken with as low a sky background as was possible. The images were typically dithered by 15 pixels, with additional sub-pixel dithers applied. Apart from a variety of short exposures (durations ranging from 1s to 40s) used to treat the brighter stars, the deep exposures were of similar duration and were thus assigned equal weight in the analysis. The full details of the analysis will be described elsewhere (Anderson et al 2007) but we review here the aspects thereof that are directly relevant to the identification of the faint point sources that make up the white dwarf cooling sequence.

Essentially, our approach uses the fact that the only influence the faintest stars will have on the image is to push their central pixels up above the noise in some number of the images. If a star is not bright enough to do this, then there is no way it will be found. However, if it does manage to generate a local maximum in a statistically significant number of images, then one can find it by searching for coincident peaks, peaks that occur in the same place in the field in different exposures. After much experimentation (including artificial star tests), it was determined that a star must generate a peak in at least 90 out of the 252 F814W images to qualify as a 99% significance detection (the inclusion of the F606W images did not increase the significance levels).

Thus, we generate a list of possible sources by identifying every place in the field where a peak was found in at least 90 F814W images. To suppress artifacts around bright stars, we also require that the source be the most significant concentration of peaks within 7.5 pixels. This initial pass results in a catalog of 48,785 potential sources. Inspection of these sources on a stacked image shows that while this procedure identifies everything that is visibly a star, it also nets plenty of artifacts and galaxies.

We measure each of these sources as if it was a star, using a careful PSF-fitting procedure to get a position and a flux in F606W and F814W. We then use a three-pronged weeding procedure to remove the non-stellar objects. The first two procedures target the PSF artifacts. While the 7.5-pixel halo removes a lot of such artifacts, there are many PSF features that extend beyond this radius. A spike filter is applied to the stacked image to identify the likely contribution of diffraction spikes to every point in the field. We require that each identified source be much brighter than the expectation value of spikes at its location. The second weeding step examines the brightness of a source in relation to its brighter neighbors. Artifacts exhibit a clear relationship between their distance from a bright star and their own brightness. We create a halo around each bright star that tells us how bright a faint star must be to be believable. Both of these tests are detailed in Anderson et al (2007).

The above cuts remove the instrumental artifacts but still include real astrophysical objects (i.e. galaxies) that we wish to discount. In order to restrict our sample to point sources we make two further morpho-

logical cuts.

2.1. Star-Galaxy Separation

The first cut compares the flux in the central pixel to the overall flux extracted from the PSF model for the star. From this we measure the fractional central pixel excess/deficit, hereafter termed **CENXS**. A deficit indicates that the object is partially resolved and thus extended. A similar measure (**ELONG**) can be made for the residual asymmetry in the image within 1.5 pixels radius. Larger asymmetries again suggest that the object is resolved. On this basis we can remove all the partially resolved objects, leaving us with a sample of 8399 potential point sources.

The last cut made is to exclude a region of radius 180 pixels around an apparent concentration of faint blue sources located at $(x,y)=(725,720)$ on the chip. It turns out that there is a large elliptical galaxy located near that position. Thus these objects are most likely not white dwarfs but rather globular clusters associated with the galaxy. Most of these fall outside the colour-magnitude range of the white dwarfs, but not all of them, and so we exclude sources in this region from our sample.

2.2. Magnitude Calibration

The conversion from instrumental to Vega magnitudes was done according to the prescription of Sirianni et al. (2005). We measure the bright stars on specific reference images in F814W (`j970101bbq_drz`) and F606W (`j970101bdq_drz`), using the standard procedure and 10-pixel radius aperture. Because this is a crowded field, we reject some of these stars for which too large a fraction of the flux was found beyond 5 pixels. This controls errors that might be introduced by either cosmic rays or other stars. These are then compared to the fluxes measured using our PSF-fitting procedure to determine the zero-point for our calibration. The sigma-clipped average of this comparison yields $ZP(F606W)=33.321$ and $ZP(F814W)=32.414$.

Figure 1 shows the final colour-magnitude diagram that results. The main sequence of the cluster is clearly seen, from above the turnoff to where the contrast with the background population fades near the hydrogen burning limit. Most exciting for the purposes of this paper, is the very clear cooling sequence of the cluster white dwarfs, beginning near $F814W \sim 22.5$ and extending down to an observed truncation at $F814W \sim 27.6$. The presence of a population of bluer and fainter objects (mostly the remaining unresolved galaxies but perhaps also a few background white dwarfs) in the CMD indicates that the truncation is real, and not a result of observational incompleteness. Figure 2 shows a zoom into the faint, blue region of this diagram – where white dwarfs and galaxies lie. The two panels show the effect of our galaxy–star separation. Due to the excellent image quality of the ACS data, we can identify most of the galaxies from the photometry alone. While there is certainly still some level of galaxy contamination in the point source sample, it is now at a level that can be securely modeled and included in the errors. As we will show in subsequent sections, with this data set it is possible to do model comparisons even without a proper motion separation.

2.3. Artificial Stars

An important part of the modeling effort is the need to subject the models to the same kind of observational scatter and incompleteness as the data. This is particularly important for a data set such as this,

where even relatively bright white dwarfs can be lost if they happen to be projected close to a bright main sequence star. Thus, we have performed a detailed series of artificial star tests, to measure not only the recovery fraction, but also the degree of correlation between input magnitude and observed magnitude.

Artificial stars were chosen with magnitudes and colours drawn from the canonical white dwarf cooling sequence, and added to the data on a grid, with mutual separation of ten pixels, plus a random offset of 0.5 pixels relative to the grid position. This is large enough that any given star does not affect the detectability of its neighbours. The new data set is then analysed as before and the recovery fraction measured. Figure 3 shows the resulting recovery fraction as a function of F814W. Also shown are the measured dispersions of the recovered magnitudes as a function of input magnitude. We see that, down to magnitude F814W=28, the recovery fraction is $> 50\%$ and the scatter is < 0.25 mags.

2.4. Residual Galaxy Contamination

In order to model the distribution of white dwarfs in colour and magnitude, we bin the data in the manner shown in Figure 4. As described in Hansen et al (2004) we find that the distribution of white dwarfs above the luminosity function jump (F814W ~ 26 in this case) contain very little age information, so these are added together into a single large bin. However, at fainter magnitudes, the distribution in magnitude and in colour is affected by the mass and age of the underlying white dwarfs and so there is useful information to be obtained by quantifying this distribution. Thus we bin our data on a grid in colour–magnitude space from F606W–F814W= 0.9 to 1.5 and from F814W=26 to 28.

Our definition of our data product thus far involves the cut on the CENXS and ELONG parameters to exclude extended sources, followed by binning the data as described. Before we continue to the modeling we also require a measure of the systematic error contributions to the counts in each bin. The first such contribution is from the remaining galaxy contamination in each bin. Figure 5 shows the distribution of CENXS parameter for *all* objects in the range $26 < \text{F814W} < 28$ and $0.9 < \text{F606W} - \text{F814W} < 1.5$. Hence this data set represents the distribution of all objects that fall within the colour-magnitude bounds of interest in describing the white dwarf cooling sequence. We model this as a sum of two gaussians. One, the narrow peak, represents the stellar component and the second represents the broad distribution of CENXS parameters appropriate to the partially resolved galaxy contribution. We will use this second distribution to estimate the potential contribution of unresolved galaxies to our model fits. A second contribution to systematic error comes from the fact that the counts will differ slightly if we change the particular values of the cuts on CENXS and ELONG, so we include a contribution in each bin due to a reasonable variation in the actual values of the cuts.

Table 1 shows the number counts of sources with $|\text{CENXS}| < 0.02$ in each bin along with the estimated error in each bin, including both statistical and systematic error.

2.5. An empirical cooling sequence

Before we proceed to the full modeling description, we pause to describe a procedure whereby we can derive an empirical cooling sequence, without reference to any modeling. Armed with the data and the artificial star tests, we can derive an empirical relationship between colour and magnitude under the simple assumption that the underlying relationship is monotonic – that, for any given magnitude, there is a unique

colour appropriate to the underlying cooling sequence. The observed scatter is assumed to be the result of photometric errors, quantified by the artificial star tests.

Our derivation, briefly described in Richer et al (2006), proceeds as follows. For each magnitude bin defined in Figure 4, our data consists of number counts as a function of colour. If we assume a value for the intrinsic model colour at this magnitude, we can then use the results of the artificial star tests to predict the distribution of colour (at this magnitude) expected after accounting for observational scatter. We may then characterise how well this fits with the true observed colour distribution using the χ^2 statistic. By varying the intrinsic model colour until we find the minimum of χ^2 at each magnitude, we may then derive the best fit colour as a function of magnitude – an empirical cooling sequence.

This is shown in Figure 6. This may seem superfluous given that, in subsequent sections, we’re going to fit model atmosphere colours to the data. However, there are still several issues outstanding in the chemical evolution and atmospheric modeling of white dwarfs which means that there is some uncertainty in the final model colours (Bergeron, Ruiz & Leggett 1997; Bergeron & Leggett 2002). So, it is of interest to see what kind of relationship between colour and magnitude fits the data independent of theoretical models. In particular we see evidence in Figure 6 (in the form of a turn towards the blue) for the deviation from black body trends (Hansen 1998; Saumon & Jacobsen 1999) expected due to collisionally induced absorption by molecular hydrogen in hydrogen-rich white dwarf atmospheres (Mould & Liebert 1978; Bergeron, Saumon & Wesemael 1995; Borysow, Jorgensen & Zheng 1997). Below we will see that this empirical relationship is similar to that found from theoretical hydrogen atmosphere models, suggesting that our sample is dominated by Hydrogen atmosphere dwarfs.

Furthermore, this empirical sequence should allow other groups to compare their models to the data. Table 2 gives the best fit colours as a function of magnitude.

2.6. Distance and Extinction

In both the MSTO and WDSC methods, the determination of the distance to the cluster is a fundamental aspect of the age measurement. The traditional method for globular clusters is to compare the main sequence with local, metal-poor subdwarfs with known parallaxes to determine the distance. We take our default distance to NGC 6397 to be $\mu_0 = 12.13 \pm 0.15$ by Reid & Gizis (1998), who used Hipparcos distances for the subdwarfs in V & I for their main sequence fit. This also assumes a reddening $E(B-V)=0.18$ for this line of sight. We chose this determination because most other main sequence distance determinations to NGC 6397 use the B & V bandpasses, so that the Reid & Gizis work is a more direct comparison to the bandpasses used here. We will examine this further in § 4.2.

Although we shall later compare to the distance and extinction derived from the main sequence, we prefer to initially determine these quantities directly from the white dwarf sequence. There are several reasons for this preference – for a cluster as metal poor as NGC 6397, there are very few appropriate subdwarfs and colour transformations are necessary; our observations use the F606W bandpass rather than the F555W, so that there are non-negligible colour transformations between the HST bandpasses and the ground-based bandpasses used for the distance and extinction transformation, and finally there is the fact that cool white dwarfs can have spectral shapes not well represented by the (usually much hotter) stars used to determine the reddening.

To determine the distance and extinction, we follow the same method as used in Hansen et al (2004),

essentially a variation of the distance determination method of Renzini et al (1996). An empirical fit to the upper part of the observed NGC 6397 cooling sequence is

$$\text{F814W} = 3.00 (\text{F606W} - \text{F814W}) + 23.37 \quad (1)$$

Using the atmosphere models of Bergeron et al (1995), but corrected slightly to be at fixed radius rather than fixed gravity, we get

$$(\text{F814W})_0 = 2.77 (\text{F606W} - \text{F814W})_0 + 11.51 - 5 \log R_9 \quad (2)$$

where R_9 is the white dwarf radius in units of 10^9 cm and the subscript 0 indicates the colour before reddening is applied. Taking reddening into account and assuming $A_{814} = 0.65A_{606}$ (Sirianni et al 2005), we can express the true distance modulus in terms of the other fitting parameters

$$\mu_0 = 11.86 + 0.49A_{814} + 5 \log R_9 + 0.23 (\text{F606W} - \text{F814W}) \quad (3)$$

The last term indicates that there is some small colour dependance in the fit (resulting from the fact that there is a residual difference in the slopes between equations 1 and 2). The other two parameters are the extinction and the white dwarf radius (related directly to the mass). Thus, one can trade off the distance, extinction and white dwarf mass to maintain a good fit to the observed cooling sequence. This means that the constraints on these three quantities are interrelated. Using an extinction of $A_{814} = 0.3$ (explained below), and performing the fit at $\text{F606W}-\text{F814W}=0.6$, we find the distance and radius are related by

$$\mu_0 = 12.15 + 5 \log R_9. \quad (4)$$

For a $0.5M_\odot$ white dwarf at the top of the cooling sequence, we get $\mu_0 = 12.08$, which is well within the range of acceptable distance moduli derived by Reid & Gizis. If we consider the lower limit from Reid & Gizis to be $\mu_0 > 12.0$, this restricts the range of allowed radii and hence places an upper limit on the masses at the top of the cooling sequence $M < 0.53M_\odot$.

Of course, this just means that the models and observations agree at the bright end. Much more information emerges when we consider the data at the fainter end. In the following sections, we will get constraints on the distance, extinction and masses directly from the fit to the full cooling sequence. But we can get a preview of these results in a simple way by performing an operation similar to the one above, but now for the fainter white dwarfs. In this case, the colour shift at faint magnitudes provides a feature in the cooling curve which must be fit by the observations. The most transparent way to do this is to compare our empirical cooling curve with the model curve of colour versus magnitude. Fitting a $0.5M_\odot$ model curve to the empirical sequence (Figure 6) suggests a reddening in the observed passbands of $E(\text{F606W}-\text{F814W})=0.16$. If we infer from this an extinction $A_{814} = 0.30$, then fitting a $0.5M_\odot$ white dwarf model to the data requires $\mu_0 = 12.0$, which is slightly smaller than the value derived in equation 4. The two independent measures can be made consistent if we allow the mass to increase along the cooling sequence, since the difference in the inferred μ_0 is then offset by the more negative value of the $5 \log R_9$ term for a larger mass white dwarf. By requiring that our model fit both constraints simultaneously, we are thus able to place limits on the initial-final mass relation. The fact that the change is not large also suggests that there is not a lot of variation in mass between the bottom and top of the cooling sequence, as larger mass models have smaller radii and would result in a smaller inferred μ_0 .

We will examine all of this in more detail in § 3, but the above analysis demonstrates the origin of some of our forthcoming constraints on cluster distance and white dwarf masses. It also suggests our measurements are not particularly sensitive to many of the details of the initial-to-final mass relation (which emerge mostly at the high-mass end). This will also be examined in § 4.3.

3. Models

The final data product is shown in Figures 7 and 8. In Figure 7 we show the white dwarf luminosity function using a cut $|\text{CENXS}| < 0.02$ and $\text{ELONG} < 0.02$. Figure 8 shows the binned data from the Hess diagram in colour-magnitude space using the same cuts. In Figure 7 we also show the galaxy luminosity function, which rises smoothly well beyond the observed truncation in the white dwarf luminosity function.

3.1. Default Models

We are now in a position to begin our investigation of fitting models to the full cooling sequence. Our initial fit will be to the same default model as in Hansen et al (2004). We use the white dwarf cooling models of Hansen (1999), with a hydrogen layer mass fraction of 10^{-4} and a helium layer mass fraction of 10^{-2} . We furthermore adopt an initial-final mass relation of the form (M_{TO} is the turnoff mass at a given age)

$$M_{wd} = Ae^{B(M-M_{TO})} \quad (5)$$

and we determine A and B , along with cluster distance μ_0 and extinction A_{814} , by minimizing the χ^2 of the model fit to the observations, in tandem with the determination of cluster age and progenitor mass function slope. To begin with, we take the lifetimes of main sequence progenitors from the same models as in Hansen et al (2004). We will investigate the effect of other main sequence models in § 3.2.

Using this model we generate a Monte Carlo realisation of the white dwarf population. For each white dwarf, we then add a photometric error chosen from the distribution of output magnitudes (given the intrinsic value as input magnitude) as determined from the artificial star tests. We do this for both F606W and F814W. In this manner, each realisation includes a realistic level of photometric scatter. The data is then binned in two ways. The first measure is to simply bin the F814W luminosity function in the traditional way. The second measure is to also bin the data in two dimensions (sometimes referred to as the Hess diagram) the same way as the observations, using the grid shown in Figure 4. In each case, we then perform a χ^2 fit between model and observed populations to determine the goodness of fit. To completely specify each model, we need to choose values for the age, the progenitor mass function slope x , the distance and reddening, and the two parameters A and B in equation (5). If we marginalise over these last four parameters, we find the best fit (to the Hess diagram) if we adopt the values $\mu_0 = 12.05$, $A_{814} = 0.37$ and

$$M_{wd} = 0.502M_{\odot}e^{0.101(M-M_{TO})}. \quad (6)$$

Keeping these parameters fixed, we show, in Figure 9, the confidence intervals for the fit to age and main sequence mass function slope x for this improved solution. The solid contours represent the 1, 2 and 3σ ranges obtained by fitting to the two-dimensional Hess diagram, while the dotted contours result from the fit to the luminosity function. The value of $\chi^2_{min} = 41.5$ for the Hess diagram fit corresponds to 1.34 per degree of freedom, as there are 34 total bins used in the fit. The two sigma age constraint is thus 11.7 ± 0.3 Gyr for this particular set of parameters. The comparison of the best-fit model ($T = 11.61$ Gyr, $x = 0.95$) and observations is shown in Figure 10, and is in excellent agreement overall. The one obvious disagreement that remains appears to be that the models produce a weaker turn to the blue than is found in the observations. This can be seen in the F814W= 27.25 panel in Figure 10 and also in Figure 11, which is a Monte Carlo realisation of this best fit model, plotted next to the observations. The location and width of the observed and modeled sequences are very similar, except for the weaker turn to the blue at the faint end in the models.

Also shown in Figure 9 are confidence intervals corresponding to a fit of the models to the observed luminosity function. Although the Hess fit is a more accurate measure, the historical use of the luminosity function makes this a comparison of interest. Figure 12 shows the observed luminosity function compared to the best fit model ($x = 0.59, T = 11.69$ Gyr). Also shown is the region used to perform the fit. Once again, we sum the bins with $F814W < 26$ to use as a single bin in the constraint. The constraints from the Hess diagram and the luminosity function overlap considerably, although the luminosity function, not surprisingly, offers a weaker 95% constraint on the age (11.6 ± 0.6 Gyr).

3.2. Internal Chemical Composition

One advantage the WDCS method has over the MSTO method is that the colours are not metallicity dependant in any obvious way, which means the subtleties of cluster-to-cluster variations and of the transformation from observational to theoretical planes is less fraught with peril. However, the white dwarf method is not completely free of metallicity effects. In particular, the main sequence lifetime of a given progenitor star is shorter (lower metallicity stars burn at higher temperatures and hence consume their fuel more rapidly). As a result, the models used in Hansen et al (2004) likely overestimate the main sequence lifetimes of stars as metal-poor as those in NGC 6397.

To address this problem, we use the models of Dotter & Chaboyer (based on the models of Chaboyer et al 2001), for metallicities $[Fe/H] = -2 \pm 0.1$. We have also performed fits of these same models to the main sequence turnoff (Richer et al 2007), so that our white dwarf cooling age is self-consistent with the estimates from the MSTO models (at least, to the extent that they are coupled through the progenitor lifetimes). If we repeat the procedure of § 3.1 but using these models instead, the best fit distance, extinction and mass values are given by $\mu_0 = 12.05$, $A_{814} = 0.36$ and

$$M_{wd} = 0.5M_{\odot}e^{0.169(M-M_{TO})}. \quad (7)$$

Thus, the best fit distance and extinction are quite robust, although the initial-final mass relation is steeper than before. The resulting fit for age and x is shown in Figure 13, yielding a 2σ range of 11.52 ± 0.23 Gyr from the Hess fit. The best fit Hess model has $\chi^2 = 39.6$, at $T=11.51$ Gyr. This is shown in Figure 14, and a Monte Carlo realisation of this model is shown in Figure 16. The best-fit luminosity function (at $T=11.46$ Gyr) is shown in Figure 15. The use of these new models results in a shift to a slightly lower age (although by less than the difference between the main sequence lifetimes at fixed mass in the two models) but otherwise the fits are of similar quality to before, although slightly better in this case.

Thus, the age is reduced somewhat if we use the metal-poor models of Dotter & Chaboyer, as were used in the study of the MSTO in this cluster (Richer et al 2007). However, the variation between different main sequence models is also a source of systematic error, so let us now expand our parameter study to use both these models and those of Hurley, Pols & Tout (2000), from which our default model was drawn, but now with the appropriate metallicity. In this case, we will marginalise over all the other parameters including distance, extinction, the initial-final mass relation and also x , to obtain a final, all-encompassing constraint on cluster age. The χ^2 curve is shown in Figure 17, along with the 2σ age constraint $T = 11.43 \pm 0.46$ Gyr.

Progenitor metallicities also can result in changes in the cooling models, as the nuclear burning history will affect the ratio of Carbon to Oxygen (and thus the heat capacity) in the resulting white dwarfs. The above calculations use the white dwarf compositional profiles from Hernanz et al (1994). We have also performed fits using profiles resulting from the models of Hurley et al (2000), but these result in lower χ^2

and worse fits to the data. Another possibility is that some fraction of the white dwarfs may possess Helium cores (Hansen 2005), as suggested by the strange white dwarf luminosity function of NGC 6791 (Bedin et al. 2005). However, a significant population of such white dwarfs would lead to a peak in the luminosity function at much brighter magnitudes ($F814W \sim 25.7$), which is not seen in our data. We thus conclude that NGC 6397 contains a negligible population of Helium-core white dwarfs.

3.3. Hydrogen Layer Mass

The amount of hydrogen on the surface of a white dwarf is one of the parameters that has to be specified for a white dwarf cooling model. The other models in this paper assume a Hydrogen surface layer with a total mass fraction $q = 10^{-4}$ for each white dwarf. This is the canonical value expected from standard stellar evolution, but there have been claims in the past for lower surface values. To that end, we have also performed a fit using the Dotter & Chaboyer main sequence models but now with cooling models that have thinner Hydrogen surface masses, $q_H = 10^{-6}$. The resulting fits yield worse χ^2 , even when we allow the distance, extinction and initial-final mass relation parameters to float. The minimum $\chi^2 = 55$ (for an age of 10.55 Gyr), so that we conclude that the data supports models with a standard hydrogen layer mass.

3.4. Atmospheric Composition

In the field, some fraction of white dwarfs show evidence for atmospheres whose dominant constituent is helium, rather than hydrogen. This has a marked effect on the colours at faint magnitudes, since helium atmospheres continue to redden as they get cooler, while hydrogen atmospheres get bluer (in the infrared and optical bandpasses) because of molecular hydrogen absorption. The good fit of our empirical sequence to the hydrogen model (Figure 6) suggests that the contribution of helium atmospheres is small in our case, but we can make this quantitative by including an extra parameter in our model, the fraction f_{He} of helium atmosphere white dwarfs. However, despite the addition of an extra parameter, this does not result in any improvement in the fit - essentially because helium atmosphere white dwarfs cool much faster than their hydrogen atmosphere counterparts and so smooth out the relatively sharp truncation in the luminosity function or Hess diagram. Furthermore, the colours of cool Helium atmospheres are redder than for Hydrogen atmospheres, so they do not help to alleviate the slight remaining discrepancy in the blue hook between model and observations.

3.5. Binarity

Binarity can also have an effect on the colours and magnitudes of white dwarfs. A white dwarf in a binary with a main sequence star will be overwhelmed and excluded from our sample, but two white dwarfs in a binary will add together and potentially be brighter than a single isolated star. We model this binarity by randomly selecting the progenitors from the initial mass function and then accounting for the evolution of the two white dwarfs as isolated objects, eventually summing their light in the model. The resulting simulated samples result in degraded χ^2 , indicating that there is little to no evidence for binarity in our white dwarf sample.

To illustrate this, we show in Figure 18 the effect of a given binary fraction on the χ^2 per degree of

freedom for a model with all the other parameters held fixed at the best fit values for the $Z=0.001$ model. The open circles represent fits to the luminosity function and the filled triangles represent fits to the Hess diagram. We note that the luminosity function constraints are much more strict. This is because binarity results in model stars being found in some bins in the grid where they are never found otherwise (and therefore we don't usually use these bins in our χ^2 fits because they contain no information). Thus, the open circles represent Hess fits with an expanded diagram (which feature three more bins at the bright, red end of the grid in Figure 4). This results in much stronger constraints, and we use this to quote a 2σ upper limit on the binary fraction $< 4\%$. This represents the fraction of white dwarfs that have another white dwarf as a companion.

3.6. The Main Sequence Turnoff

The traditional method for determining globular cluster ages is to fit stellar models to the main sequence turnoff. In Richer et al (2007) we compare our observations of the turnoff in this cluster to four sets of theoretical isochrones. In each case, good fits are obtained for a wide variety of ages, 12 ± 2 Gyr, where the accuracy is limited, as in prior studies, by the uncertainties in the distance and extinction. When the distance and extinction used in the MSTO method are restricted to the range that fits the white dwarf model (see § 4.2) and ages determined using the models of Dotter & Chaboyer, we find a best fit age of 11.6 Gyr, with a 95% confidence lower limit of 10.6 Gyr. Hence the two methods are in complete agreement, as these were the models used to determine the progenitor ages in Figure 13. As a result, this combination represents a successful end-to-end (main sequence to white dwarf) comparison of a set of stellar models with the observed stellar population.

4. Discussion

The fits obtained here from the white dwarf cooling sequence result in a constraint that is quite a bit tighter than the traditional MSTO method. The reason for this comes from the fact that we have modeled the entire cooling sequence, rather than just a localised feature (as in the case of the turnoff). In principle, simply fitting a cooling model to the truncation in the observed cooling sequence leads to a similarly simple constraint, but it is subject to several unsatisfactory parameter degeneracies, including those between age, white dwarf mass and cluster distance. By constructing a self-consistent model for the entire cooling sequence, these degeneracies are lifted because different choices of white dwarf mass and age have different consequences for distributions of white dwarfs in both colour and magnitude. We illustrate this by performing such a simple fit in appendix A and contrasting it with our more detailed procedure.

To arrive at a final age constraint, we have marginalised over uncertainties in distance, extinction, the white dwarf mass (and its variation along the WDCS) and binary fraction, as well as model systematics that result from different choices of main sequence models, white dwarf internal compositions and hydrogen layer masses. We have restricted our models to those of appropriate metallicity (so the models in § 3.1 are not included in the final fit) and thus our final age constraint is that derived from Figure 17, $T = 11.47 \pm 0.47$ Gyr.

To further understand which information is important in determining this constraint, let us consider the nature of the best fit models.

4.1. The Best-Fit Solution

The χ^2 value per degree of freedom for the best fit models is ~ 1.27 , so it is good, but not perfect. Figure 14 shows the level of agreement between the data and the best fit model. The model reproduces well not only the colour distributions at each magnitude, but also the normalisations at different magnitudes relative to each other. The only feature of the observations that is not well reproduced by our models is the blue colours at magnitudes $F814W \sim 27.25$. This can also be seen in the visual comparison of the two panels in Figure 16, where the models clearly do not fully reproduce the clump of stars bluewards of the faint end of the main locus. This most likely indicates some level of mismatch between the theoretical colours and the true colours at the faintest temperatures. The deviations are in the same sense as those seen in Figure 6, where the model colours lie a little lower than the empirical cooling sequence at the faint end. The fact that the blueward shift of the colours is driven by collisionally induced absorption of molecular hydrogen (Mould & Liebert 1978; Bergeron, Saumon & Wesemael 1995; Borysow, Jorgensen & Zheng 1997; Hansen 1998; Saumon & Jacobsen 1999) suggests that these deviations may indicate residual deficiencies in the models or simply that the atmospheric composition contains an admixture of Helium along with the Hydrogen. Nevertheless, we emphasize again that the model fits are still good despite this residual mismatch and that improving the colours is likely to only make the age constraint even tighter.

Let us now consider the properties of the underlying white dwarf model. Figure 19 shows the mass of the white dwarf as a function of F814W magnitude for the best-fit solution. Note, the F814W magnitude shown in this plot does not include the photometric scatter. In the upper panel we show the observed luminosity function, to indicate the range over which the cutoff occurs. The white dwarfs in this part of the luminosity function range from $0.52M_{\odot}$ to $0.62M_{\odot}$. This is important, because it means the more massive white dwarfs do not contribute significantly to the luminosity function. This is because they cool faster at late times (as can be seen by the flattening in the F814W- M_{wd} curve). A consequence of this is that we cannot directly interpret the cluster age as the white dwarf cooling time, because even the white dwarfs at the start of the truncation come from relatively low-mass main sequence stars, and therefore have a small contribution to the total age from the main sequence lifetime. This is shown explicitly in Figure 20 where we show a similar diagram to Figure 19 but we now show the main sequence mass, related to the white dwarf mass through the initial-final mass relation. Also shown is the corresponding main sequence lifetime from the Dotter & Chaboyer models. We see that the truncation in the white dwarf luminosity function appears when the main sequence age of the progenitors starts to drop precipitously, so that we get older, cooler and fainter white dwarfs. Over a range of only 0.5 magnitudes, we see that the cooling time of the white dwarfs at these magnitudes changes by > 5 Gyrs! This is the ultimate source of the truncation – a bin of fixed width in magnitude corresponds to a much smaller range in the progenitor mass function than higher up the cooling sequence, and so there are fewer stars in that bin. The underlying physical reason for this is that more massive white dwarfs initially cool more slowly because they have larger heat capacity, but they crystallise earlier because of the high central densities and thereafter cool more quickly as the heat capacity enters the Einstein-Debye regime. This means that, at any given age, there is a ‘leading edge mass’, above which the white dwarfs have overtaken their less massive counterparts, and cooled beyond detection.

We can now also return to the issue of how the luminosity function truncation is affected by incompleteness. Figure 21 shows the luminosity function taking into account the observational incompleteness (solid histogram) and the corresponding complete luminosity function (dashed histogram). We see that the sharp drop is a direct consequence of the model, and not strongly affected by observational incompleteness, even at $F814W \sim 28$, where the recovery fraction is only 53%. The reason for this is that we lose white dwarfs primarily through confusion with brighter stars, not because of large photometric scatter from noise in those

that we do recover. To understand this better, consider Figure 22, in which we show the results of artificial star tests for stars inserted with $F814W=27.9$. The fraction of stars never recovered at all is 47%, but the dispersion of those that are recovered is only ~ 0.1 magnitudes. This is not sufficient to alter the shape of the recovered luminosity function.

As a final demonstration of the properties of our modelling procedure, we show in Figure 23 the effect on the model population as we change the age. The middle panel shows the best-fit model from Figure 16 and the left and right panels show the same model but for ages of 10 Gyr and 13 Gyr, with all other parameters held fixed. The younger population is clearly distinguishable from the best-fit model, with a truncation at brighter magnitudes (the $\chi^2 = 171$ for this model). The population at 13 Gyr shows no abrupt edge except that due to incompleteness at $F814W > 28$, and a much stronger colour evolution ($\chi^2 = 185$).

4.2. Distance Scale and Extinction Redux

The shaded region in Figure 24 shows the 2σ range for NGC 6397 distance modulus and reddening, for the fit to the Dotter & Chaboyer models. This is compared to the equivalent values from three studies determined by comparing the main sequence with field M-subdwarfs measured by Hipparcos. The solid point is the value obtained by Reid & Gizis (1998), which is probably the most easily compared to our value, since the comparison was made in the V & I bands. Indeed, our value is consistent with the low end from that study. The value obtained by Reid (1998), used the B & V bands, is shown as the open circle, and is somewhat higher than our white dwarf distance. The best agreement is obtained with the value quoted by Gratton et al (2003), obtained again using the B & V bandpasses, but with a variety of assumptions regarding colour corrections etc that differ from those of Reid. In fact, our distance is somewhat better constrained than the main sequence values, yielding $\mu_0 = 12.03 \pm 0.06$ at 2σ , while the reddening is constrained to be $E(F606 - F814) = 0.20 \pm 0.03$.

4.3. Initial-to-Final Mass Relation

One of the inputs into our model is the relationship between the white dwarf mass and the mass of its progenitor. This is a fundamental quantity that has been studied for many years, so it is natural to ask how our best model fits correspond to those determined empirically. Figure 25 shows two of our fits (using our default models and then the metal-poor Dotter & Chaboyer fits in § 3.2) compared to a well-known empirical IFMR from Weidemann (2000) and a more recent fit from Ferrario et al (2005). It is encouraging that our best fit model recovers a relation similar to the empirical ones, although it must be noted that our fit really only probes a limited range of masses, as inferred from Figure 19, essentially the unshaded region in Figure 25. We note also that our IFMR is in agreement with the results of Moehler et al (2004), who found, using multicolour photometry, that the mean mass of white dwarfs at the top of the cooling sequences in NGC 6397 and NGC 6752 was $0.53 \pm 0.03M_{\odot}$. This is also in agreement with theoretical expectations (Renzini & Fusi Pecci 1988).¹³

¹³Renzini & Fusi Pecci make a second prediction which could, in principle, be constrained by our results. They predict a very small dispersion in the white dwarf mass $\sigma_M \sim 0.003M_{\odot}$, which should translate into a dispersion in magnitude at fixed colour on the upper part of the cooling sequence. Our measured dispersion for white dwarfs with $F814W < 25$ is $\sigma_{814} = 0.095$ (measured as the dispersion about the best fit linear trend on the upper cooling sequence). This translates to a variation in white dwarf radius of $\delta R/R = 0.044$, and so $\sigma_M \sim 0.066M_{\odot}$. It is an order of magnitude larger than the prediction and larger

4.4. Cosmological Considerations

One of the more exciting aspects of this result is that we get a finite upper limit on the age. Most other measurements, including our M4 result, yield primarily lower limits on the age of star clusters when the full systematics are taken into account. The reason for the excitement is that we can now start to properly constrain the cosmological epoch at which NGC 6397 formed.

Let us consider a flat universe with a cosmological constant and parameterised by the present day matter density Ω_0 . The present-day age for an object formed at redshift z_c is (Weinberg 1989)

$$T(z_c) = \frac{2}{3} \left[1 + \frac{\Omega_0}{1 - \Omega_0} \right]^{1/2} H_0^{-1} \left(\sinh^{-1} \left[\frac{1 - \Omega_0}{\Omega_0} \right]^{1/2} - \sinh^{-1} \left[\left(\frac{1 - \Omega_0}{\Omega_0} \right)^{1/2} (1 + z_c)^{-3/2} \right] \right) \quad (8)$$

where H_0 is the present-day Hubble constant (which we will take to be $71 \text{ km.s}^{-1}.\text{Mpc}^{-1}$). Using the parameters from the best fit cosmologically flat model to the microwave background anisotropy (Spergel et al 2003), we take $\Omega_0 = 0.27$, which gives a present day age of 13.7 Gyr for the universe. We can use equation (8) to figure out the range of possible formation redshifts, given the age of NGC 6397, which we take to be 11.47 ± 0.47 Gyr (our 2σ value). The resulting formation redshift is

$$z_c = 3.1 \pm 0.6. \quad (9)$$

Figure 26 shows this result compared to the relation (8) for the WMAP cosmology. Our result places the formation epoch of NGC 6397 somewhat more recently than the reionization epoch (generally taken to be at redshifts of 6 or greater) but quite naturally associated with the copious star formation seen at redshifts $\sim 2 - 4$. As noted above, we are in agreement with prior age estimates for the Globular Cluster system based on the MSTO method but those estimates could only place a lower limit on the age of the system. The greater precision of our method now allows us, for the first time, to determine a realistic offset between the creation of the universe and the formation of the globular cluster system, while also confirming the significant delay between globular cluster formation and the onset of star formation in the Galactic disk that we found in Hansen et al. (2002).

The age for NGC 6397 places its origin firmly near the peak of the cosmic star formation rate, as measured by various deep cosmological surveys (Madau et al 1996; Thompson et al 2006), shown in Figure 27. The origins of globular clusters has been a subject of debate for at least forty years. The first proposed scenarios postulated a very early origin (Peebles & Dicke 1968; Fall & Rees 1985) although the possible role of mergers was also recognised (Searle & Zinn 1978; Schweizer 1987; Ashman & Zepf 1992). The position of globular clusters within the modern hierarchical structure paradigm is highly uncertain, and our age determination now offers the opportunity to draw a distinction between at least some of the competing proposals. With a formation redshift $z \sim 3$, NGC 6397 appears to have formed after the epoch of reionization, which is conservatively held to be at $z > 6$ (Fan, Carilli & Keating 2006). If we assume NGC 6397 is representative of the class of metal-poor globular clusters as a whole, this rules out the notions that cluster formation was triggered by radiation pressure-driven collapse in protogalactic haloes during reionization (Cen 2001) or that the clusters were themselves responsible for the reionization (Ricotti 2002). Furthermore, the

than the scatter in the photometry at these magnitudes. We might infer a larger dispersion in mass than expected, although there are other possible contributions such as variations in hydrogen layer mass and spectral composition (DB stars have smaller radii). It is worth noting though, that this width is narrower than the estimated width of the field sample $\sigma_M = 0.137M_\odot$ (Bergeron, Saffer & Liebert 1992).

age of NGC 6397 seems inconsistent with the notion of Forbes et al (1997) that the metal-poor clusters formed early and were ‘switched off’ by some later event, possibly reionization (Santos 2003). Our results are much more consistent with scenarios that associate cluster formation with the epoch of rapid, starburst-driven star formation that occurs at $z \sim 2-3$, be it by gas collapse in dense, gaseous disks of high redshift galaxies (Kravtsov & Gnedin 2005) or collapse driven by starburst winds compressing the gas in accreting satellites (Scannapieco, Weisheit & Harlow 2004).

Of course, we base these inferences on a single cluster. The role of NGC 6397 as a tracer of the earliest star formation epoch in our galaxy is based on its low metallicity. The orbit, however, is not exactly what one might expect from a true halo object (Milone et al 2006; Kalirai et al 2007), never getting more than 3 kpc above the galactic plane. Although MSTO methods place the ages of the outer globulars as consistent with that of NGC 6397 (e.g. Salaris & Weiss 2002) the 2σ accuracy of the method (~ 1.5 Gyr) means the constraint is much less stringent than our absolute age measurement.

4.5. Outlook

The age constraint we derive is more precise than those of previous studies using the MSTO method, and also more precise than our earlier result on M4 (Hansen et al 2004). In our M4 study we also tried to calculate ages using other white dwarf models from the literature. We have not done so in this study because we now require knowledge of the models in more detail than can be gleaned from published material. We hope that other groups will perform similar analyses using their models, so that we may gain a more realistic understanding of the systematic uncertainty in the age based on using different evolutionary codes. We caution, however, that simple heuristic, comparisons between models and observations are unlikely to yield particularly interesting answers, as can be seen from appendix A. To aid in proper comparison, we include in Tables 3 and 4 the results of our artificial star tests, in which we quantify the amount of photometric scatter that results as a function of intrinsic magnitude. Feeding theoretical models through this matrix and then comparing to the data in Table 1, one can perform statistically well-posed fits between models and data.

The prospects of extending this methodology to other clusters is somewhat limited by the extreme faintness of the coolest white dwarfs. The only other clusters for which this seems feasible are NGC 6752 and 47 Tucanae. Nevertheless, similar observations of these clusters could be very illuminating, as this trio represent the archetypes for the metal poor, intermediate metallicity and metal-rich/thick disk/Bulge cluster families. In particular, NGC 6397 and NGC 6752 are considered contemporaneous by MSTO age determinations, while 47 Tuc may be marginally younger (e.g. Sarajedini, Chaboyer & Demarque 1997; Rosenberg et al 1999; Gratton et al 2003). The white dwarf cooling sequence offers us then the chance to test these assertions at greater accuracy. However, the observational expense involved in such projects will prevent similar tests in more distant clusters.

One other important outlook is to confirm our method of background subtraction by repeating this analysis with a true proper motion-selected sample, all the way down to the cluster cooling sequence truncation. This will be performed in the coming year, in HST program GO-10850. While we are confident that the gross features of the white dwarf population as outlined here will remain the same, a proper motion selection will shed important new light on the less populated parts of the colour-magnitude diagram. In particular, we anticipate the discovery of a tail of higher-mass white dwarfs fainter and bluer than the bulk, which are presently confused with the residual galaxy population. Such a tail will help us to understand whether the

residual differences between the observed and model populations are a consequence of a colour mismatch or a missing piece of physics.

5. Conclusion

In conclusion, we have performed a detailed Monte-Carlo simulation of the white dwarf population in the metal-poor globular cluster NGC 6397, comparing it to the observed WDCS obtained with the ACS camera on HST. The principal conclusion that results from this comparison is that the age of the cluster is 11.47 ± 0.47 Gyr at 95% confidence. NGC 6397 is a member of the class of metal-poor clusters that are thought to be amongst the oldest objects in the Milky Way and so this age places the epoch of original assembly of the Galaxy at $z = 3.1 \pm 0.6$.

Our model is also in agreement with various independent measures of several of the parameters, such as the distance and extinction along the line of sight, and the relationship between white dwarf mass and progenitor mass.

BH, JA, RMS, IK & MMS acknowledge support from proposal GO-10424, and JK is supported through Hubble Fellowship grant HF-01185.01-A, all of which were provided by NASA through grants from the Space Telescope Science Institute, which is operated by the Association of Universities for Research in Astronomy, Inc., under NASA contract NAS5-26555. HBR also acknowledges the support of the US-Canada Fulbright Fellowship Committee. The research of HBR & GGF is supported in part by the Natural Sciences and Engineering Research Council of Canada.

REFERENCES

- Anderson, J. et al., 2007, in preparation
- Ashman, K. M. & Zepf, S. E., 1992, *ApJ*, 384, 50
- Bedin, L., Salaris, M., Piotto, G., King, I. R., Anderson, J., Cassisi, S. & Momany, Y., 2005, *ApJ*, 624, L45
- Bergeron, P. & Leggett, S. K., 2002, *ApJ*, 580, 1070
- Bergeron, P., Ruiz, M. T. & Leggett, S. K. 1997, *ApJS*, 108, 339
- Bergeron, P., Saffer, R. A., & Liebert, J., 1992, *ApJ*, 394, 228
- Bergeron, P., Saumon, D. & Wesemael, F., 1995, *ApJ*, 443, 764
- Bergeron, P., Wesemael, F. & Beauchamp, A., 1996, *PASP*, 107, 1047
- Bolte, M. C. & Hogan, C. J., 1995, *Nature*, 376, 399
- Borysow, A., Jorgensen, U. G. & Zheng, C., 1997, *A&A*, 324, 185
- Cen, R., 2001, *ApJ*, 560, 592
- Chaboyer, B. C. et al., 2002, in *Science with the Space Interferometry Mission*, ed. S. Unwin & S. Turyshev, p. 12
- Chaboyer, B. C., Demarque, P., Kernan, P. J. & Krauss, L. M., 1998, *ApJ*, 494, 96
- Chaboyer, B. C., Fenton, W. H., Nelan, J. E., Patnaude, D. J. & Simon, F. E., 2001, *ApJ*, 562, 521

- Chieffi, A., & Straniero, O., 1989, *ApJS*, 71, 47
- de Marchi, G., Paresce, F., Straniero, O. & Prada Moroni, P. G., 2004, *A&A*, 415, 971
- Fahlman, G. G., Richer, H. B. & Vandenberg, D. A., 1985, *ApJS*, 58, 225
- Fall, S. M. & Rees, M. J., 1985, *ApJ*, 298, 18
- Fan, X., Carilli, C. L. & Keating, B., 2006, *ARA&A*, 44, 415
- Ferrario, L., Wickramasinghe, D., Liebert, J. & Williams, K. A., 2005, *MNRAS*, 361, 1131
- Forbes, D. A., Brodie, J. P., & Grillmair, C. J., 1997, *AJ*, 113, 1652
- Janes, K. & Demarque, P., 1983, *ApJ*, 264, 206
- Gratton, R. G., Bragaglia, A., Carretta, E., Clementini, G., Desidera, S., Grundahl, F. & Lucatello, S., 2003, *A&A*, 408, 529
- Hansen, B. M. S., 1998, *Nature*, 394, 860
- Hansen, B. M. S., 1999, *ApJ*, 520, 680
- Hansen, B. M. S., et al., 2002, *ApJ*, 574, L155
- Hansen, B. M. S., et al., 2004, *ApJS*, 155,551
- Hansen, B. M. S., 2005, *ApJ*, 635, 532
- Harris, H. C., et al., 2006, *AJ*, 131, 571
- Hernanz, M. et al, 1994, *ApJ*, 434, 652
- Hurley, J. R., Pols, O. R. & Tout, C. A., 2000, *MNRAS*, 315, 543
- Hurley, J. R. & Shara, M. M., 2003, *ApJ*, 589, 179
- Kalirai, J., et al., 2007, *ApJ*, submitted
- Krauss, L. M. & Chaboyer, B., 2003, *Science*, 299, 65
- Kravtsov, A. V. & Gnedin, O. G., 2005, *ApJ*, 623, 650
- Leggett, S. K., Ruiz, M. T. & Bergeron, P., 1998, *ApJ*, 497, 294
- Madau, P. et al., 1996, *MNRAS*, 283, 1388
- Milone, A. P., Villanova, S., Bedin, L. R., Piotto, G., Carraro, G., Anderson, J., King, I. R., & Zaggia, S., 2006, *A&A*, 456, 517
- Moehler, S., Koester, D., Zoccali, M., Ferraro, F. R., Heber, U., Napiwotzki, R. & Renzini, A., 2004, *A&A*, 420, 515
- Mould, J. & Liebert, J., 1978, *ApJ*, 226, L29
- Oswalt, T. D., Smith, J. A., Wood, M. A. & Hintzen, P. M., 1996, *Nature*, 382, 692
- Peebles, P. G. & Dicke, R. H., 1968, *ApJ*, 154, 891
- Pols, O., Schroder, K., Hurley, J., Tout, C. & Eggleton, P., 1998, *MNRAS*, 298, 525
- Reid, I. N. & Gizis, J. E., 1998, *AJ*, 116, 2929
- Reid, I. N., 1998, *AJ*, 115, 204
- Renzini, A. et al., 1996, *ApJ*, 465, L23
- Renzini, A. & Fusi Pecci, F., 1988, *ARA&A*, 26, 1999

- Riccotti, M., 2002, MNRAS, 336, L33
- Richer, H. B., *et al.*, 2004, AJ, 127, 2904
- Richer, H. B., *et al.*, 2006, Science, 303, 936
- Richer, H. B., *et al.*, 2007, in preparation
- Rosenberg, A., Saviane, I., Piotto, G. & Aparicio, A., 1999, AJ, 118, 2306
- Salaris, M. & Weiss, A., A&A, 335, 943
- Sandage, A. R., 1953, AJ, 58, 61
- Santos, M., 2003, in ‘Extragalactic Globular Cluster Systems’, ed. M. Kissler-Patig (Garching: ESO), 345
- Sarajedini, A., Chaboyer, B. & Demarque, P., 1997, PASP, 109, 1321
- Saumon, D. & Jacobsen, S. B., 1999, ApJ, 511, L107
- Scannapieco, E., Weisheit, J. & Harlow, F., 2004, ApJ, 615, 29
- Schweizer, F., 1987, in ‘Nearly Normal Galaxies: From the Planck Time to the Present’, ed. S. Faber, 18 (New York: Springer-Verlag)
- Searle, L. & Zinn, R., 1978, ApJ, 225, 357
- Sirianni, M. *et al.*, 2005, PASP, 117, 1049
- Spergel, D. N., *et al.*, 2003, ApJ, 148, 175
- Thompson, R. I., *et al.*, 2006, ApJ, 647, 787
- Vandenberg, D. A., Bolte, M. A. & Stetson, P. B., 1996, ARA&A, 34, 461
- Weidemann, V., 2000, A&A, 363, 647
- Weinberg, S., 1989, Rev. Mod. Phys., 61, 1
- Winget, D. *et al.*, 1987, ApJ, 315, L77
- Wood, M. A., 1992, ApJ, 386, 539
- Zoccali, M. *et al.*, 2001, ApJ, 553, 733

A. A Simple fit to the Cooling Sequence Truncation

In this appendix, we perform a simple-minded comparison between our cooling models and the observed truncation of the white dwarf sequence. Although our full model comparison results in much tighter constraints, this exercise is still instructive as it further illustrates how some of the ancillary information is used in the proper models.

As a first step, we characterise the magnitude of the truncation as $F814W = 27.6 \pm 0.1$. Using the distance and extinction from Reid & Gizis (1998), we convert this into an absolute magnitude $M_{814} = 15.15 \pm 0.15$. We can thus compare this to a model to infer an age. However, we first need to specify the mass of the white dwarf, and this is a free parameter in the absence of other constraints. Figure 28 shows the absolute magnitude as a function of age of Hydrogen atmosphere models of various masses. A further constraint is included, requiring that the $F606W-F814W$ colour of the models lie in the range 1.13 ± 0.13 (the dereddened

colour range spanned by the observations at the location of the truncation). Those parts of the curve that meet this criterion are solid, while those that do not are dashed. We see that acceptable ages are found for all masses, the cooling age increasing for masses from $0.5M_{\odot}$ to $0.65M_{\odot}$ and then decreasing thereafter (because of the faster cooling – due to core crystallisation – of more massive white dwarfs at late times). Thus, in the absence of other information, we infer an age range 10.2 ± 1.4 Gyr (cooling age only).

The reason that the full models yield a precise value is because they incorporate other constraints. Most notably, the models have to fit the location of the cooling sequence at the bright end (which favour models in which the white dwarfs have masses $< 0.55M_{\odot}$ initially). With this additional constraint, the shape of the observed cooling sequence constrains how much the mass can vary along the cooling sequence and the manner in which the numbers increase along the sequence constrains which cooling models and which masses yield good fits. Finally, this full modelling approach also incorporates the main sequence lifetime, which contributes about 5-10% to the final age for stars at $F814W=27.6$ in the best fit model (this can be seen by comparing Figures 20 and 28.)

Thus, we can build a rough picture of where the final number comes from. Our best-fit models suggest the white dwarf mass at the truncation is $\sim 0.6M_{\odot}$, which corresponds to a cooling age of $\sim 11.0 \pm 0.5$ Gyr, according to Figure 28. The initial-final mass relation emerging from the fit yields a progenitor mass $\sim 2M_{\odot}$, which in turn yields a main sequence lifetime ~ 0.5 Gyr. Thus, we arrive at a cluster age $\sim 11.5 \pm 0.5$ Gyr.

B. Proper Motions

Approximately 54% of our ACS field has some prior WFPC2 imaging, so proper motion separation is, in principle, possible. However, the first epoch exposures are not deep enough to allow us to perform proper motion separation at a level necessary to reach the end of the white dwarf cooling sequence.

Figure 29 shows the proper motion displacement (μ , in units of ACS pixels) for all point sources (all objects in Figure 1) as a function of $F814W$ magnitude. This is done by matching each ACS detection to the closest 2σ peak in the WFPC2 data. This works well for magnitudes $F814W < 26$, leading to a very clear separation of the cluster ($\Delta\mu < 1.5$ pixel) and Galactic field stars ($1.5 < \mu < 5$ pixels). However, we can see that, at magnitudes $F814W > 26.5$ there is a very incomplete separation of the cluster stars. There is clearly still a clump at small μ , but the distribution of μ is large and consistent with noise.

C. Cluster Dynamical Effects

NGC 6397 is a post core-collapse cluster. At the high central densities experienced in this cluster, many exotic dynamical interactions can occur between stars. Stars in binaries can be ejected, single stars can be exchanged into binaries and mass transfer between stars can be either halted or initiated. It is thus natural to wonder whether such processes have any effect on our parameter estimation.

The first thing to note, of course, is that our field is chosen to minimise contributions of this kind, since it is located well away from the high density core. Nevertheless, mass segregation is an important process in globular clusters and some stars with exotic evolutionary histories may be able to migrate outwards far enough to enter our sample. To examine this possibility, we have examined an N-body simulation of NGC 6397, calculated in the manner described in Shara & Hurley (2006). The simulation began with 100,000 stars, 5% of which were in binaries initially. The model cluster reached core collapse at 15 Gyr,

with 25,000 stars remaining, so its late-time structure is qualitatively similar to that observed for NGC 6397. Our modeling procedure is already able to treat a binary population and our data also show little or no evidence for binarity. The bigger worry is that we are not modeling the age distribution of white dwarfs properly because of the contribution of so-called ‘divorced’ white dwarfs – stars that spent some time in a binary, experienced mass transfer which altered the stellar evolution ‘clock’, and were then removed from the binary by a dynamical interaction. It is these stars that are not necessarily so easy to identify directly, since the only way they will stand out from the regular cooling sequence is if there is a sufficiently large mass difference with similar age white dwarfs from single star evolution (‘bachelor’ white dwarfs) to make a measureable difference in the photometry. Given the telescoped nature of the initial-final mass relation, this is not a very sensitive test.

The upper panel of Figure 30 shows the radial distribution of bachelor and divorced white dwarfs from the Hurley & Shara simulation at an age of 13 Gyr. We see that the divorced white dwarf profile is essentially a scaled version of the bachelor radial profile. The scaling factor is $\sim 7\%$ i.e. at any radius, the divorced white dwarfs make up roughly 7% of the white dwarfs. The lower panel shows the age distribution of the divorced white dwarfs (points) compared to a scaled version of the bachelor age distribution. Once again, there is excellent agreement, suggesting that the degree of dynamical interaction and mass transfer is not sufficient to dramatically alter the stellar evolution clock. The one potential discrepancy is a 2σ excess of white dwarfs with $T_{wd} < 200$ Myr i.e. divorced white dwarfs that were born anomalously early. However, even if this is real, the excess corresponds to roughly 5% of the divorced white dwarfs, which are themselves a minority population. Overall, this corresponds to roughly 3 anomalously young white dwarfs per sample of 1000. This is far too little to have any effect on our results.

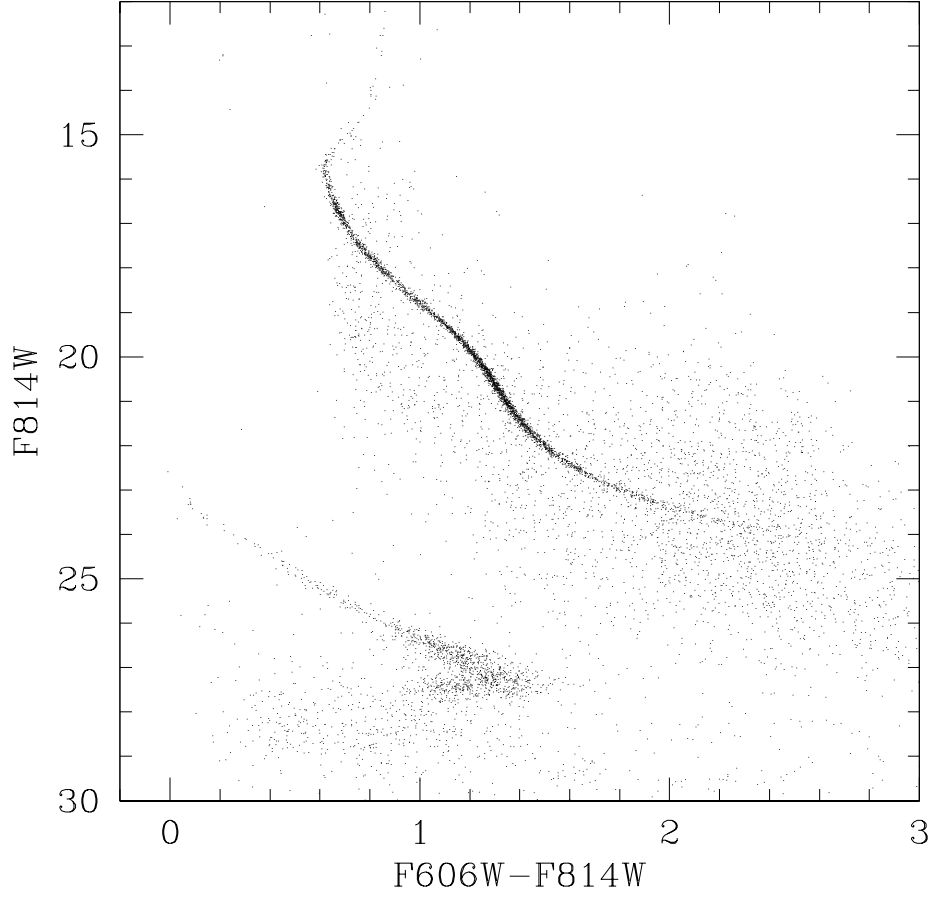


Fig. 1.— The ACS colour-magnitude diagram for our field in NGC 6397. All real point sources are shown (so the extended galaxy population is not shown). Prominent features include a cluster main sequence, a clear Main sequence turnoff and a clear white dwarf cooling sequence. Most important is the clear evidence for a sharp decline in the number of white dwarfs at magnitudes greater than $F814W=27.6$. The detectability of sources at fainter magnitudes is evident from the fainter, bluer population of background galaxies that survive the point source cuts.

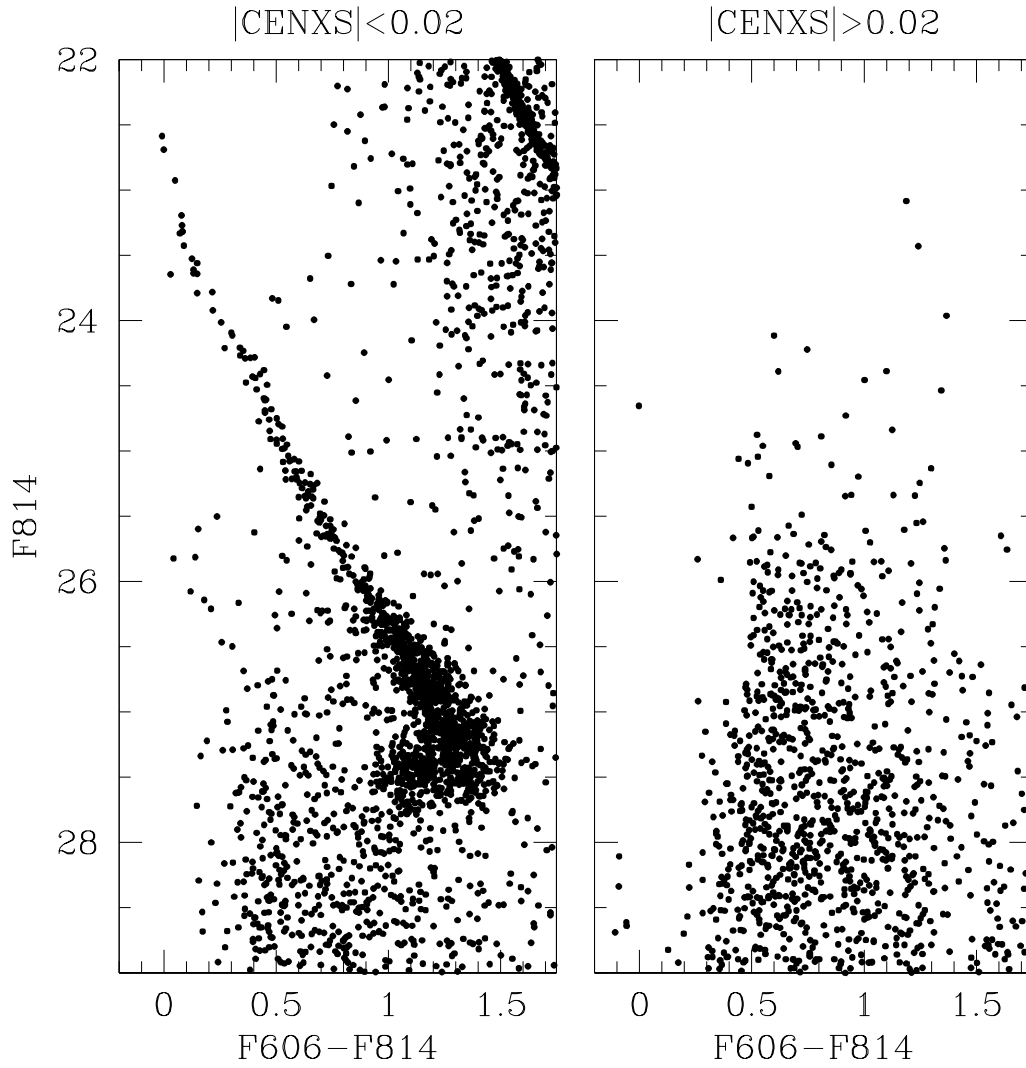


Fig. 2.— The left hand panel shows the point sources in the region of the colour magnitude diagram that encloses the white dwarf population. The right hand panel shows the full population of extended sources in the same region – this is the background galaxy population.

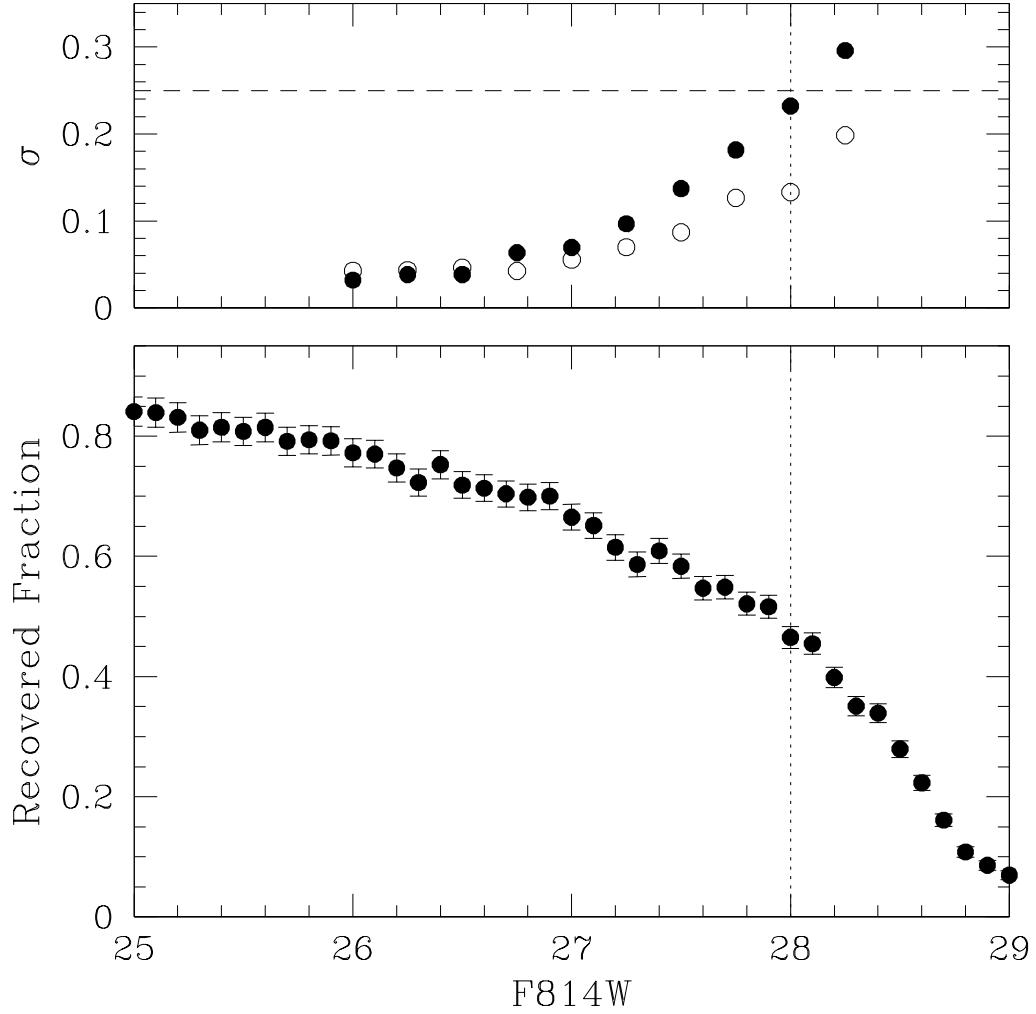


Fig. 3.— The lower panel shows the recovery fraction of artificial white dwarfs as a function of F814W magnitude. The upper panel shows the dispersion in the recovered magnitudes. The distribution is asymmetric with respect to stars recovered at fainter/greater magnitudes (solid points) and brighter/smaller magnitudes (open points) and so the dispersions are fit independently. The vertical dotted line indicates an input magnitude F814W=28 and the dashed line shows a magnitude of 0.25 mags.

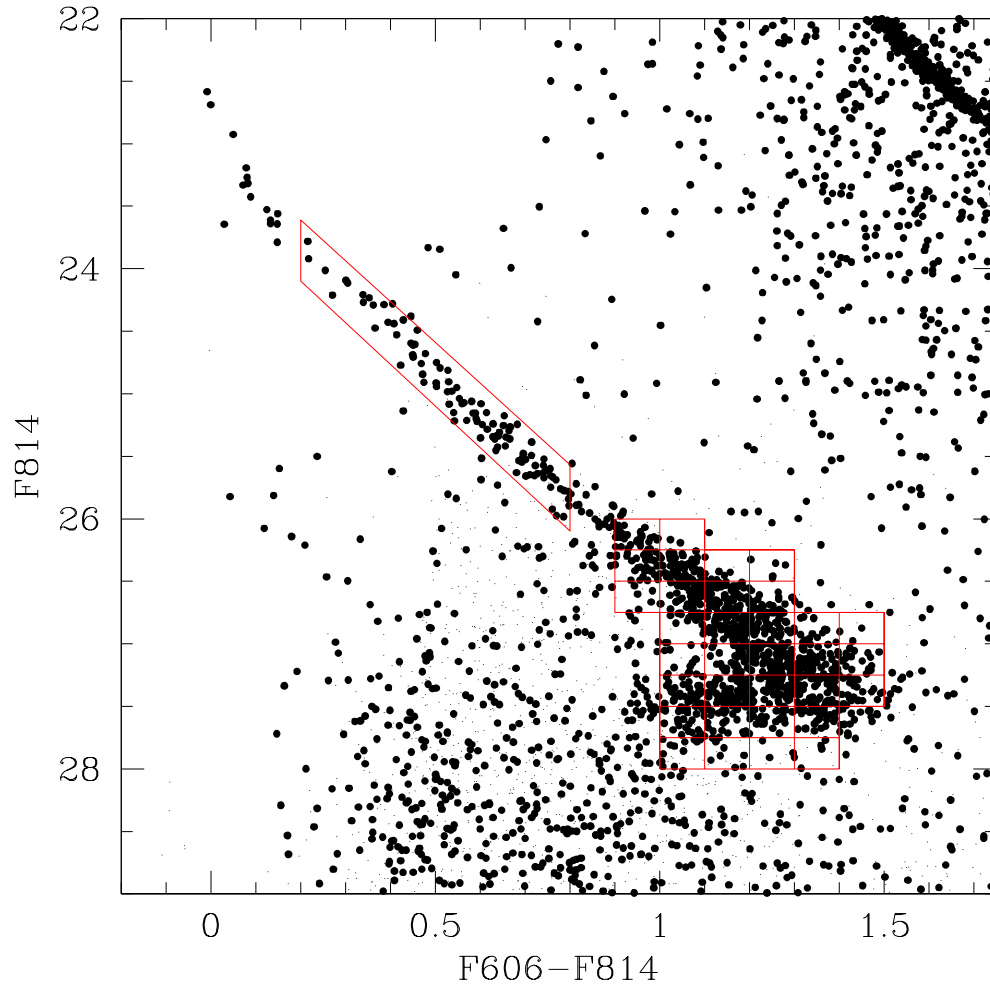


Fig. 4.— The red grid overlaid on the white dwarf population indicates the manner in which we will bin the results for comparison to the models. The small points show the location of extended sources.

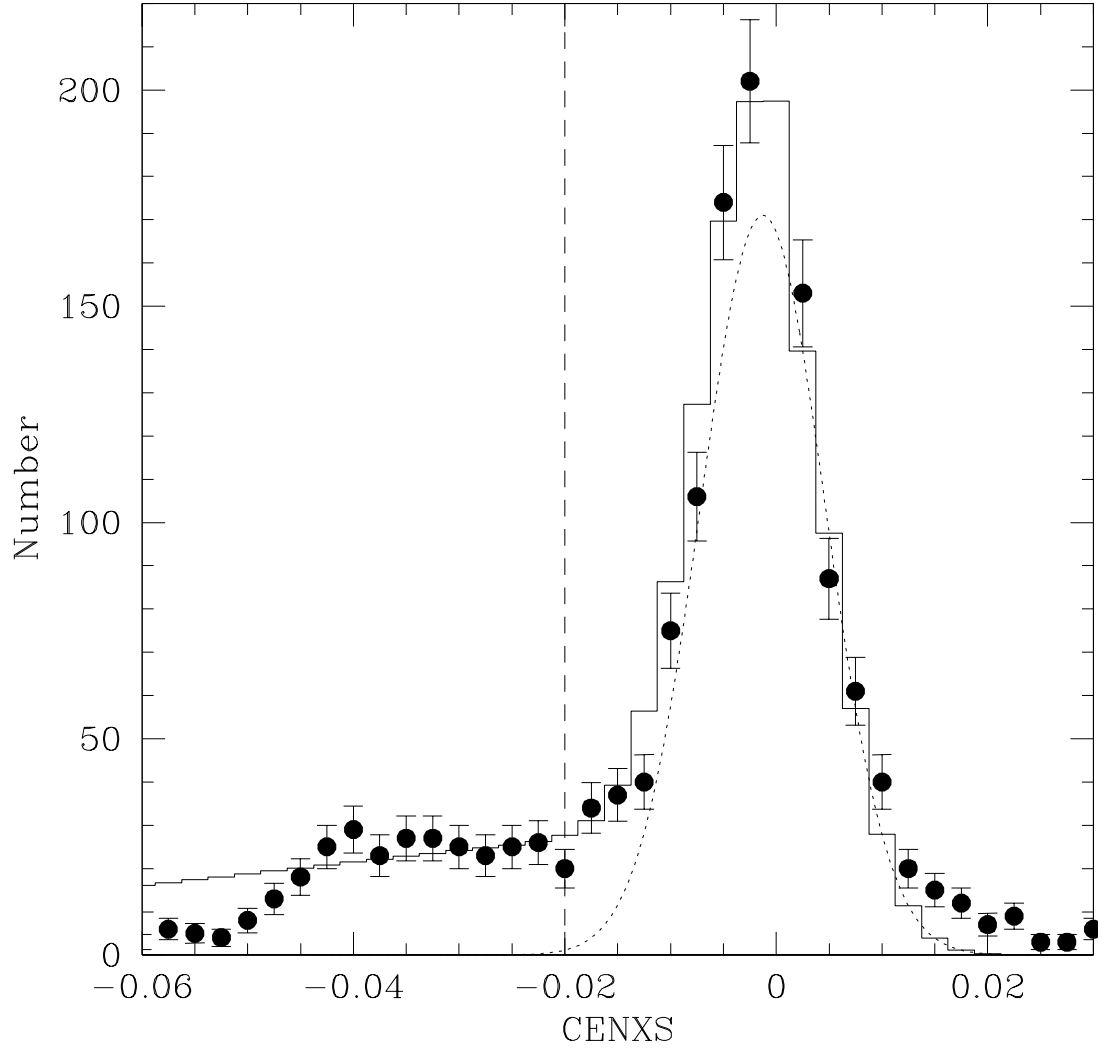


Fig. 5.— The solid points indicate the distribution of the **CENXS** parameter for all objects that fall within the grid we use to analysis the white dwarf luminosity function. The dotted curve indicates the best fit gaussian distribution to the main peak of stellar objects. The solid histogram includes both this and a second (one-sided) gaussian to represent the partially resolved galaxy contribution.

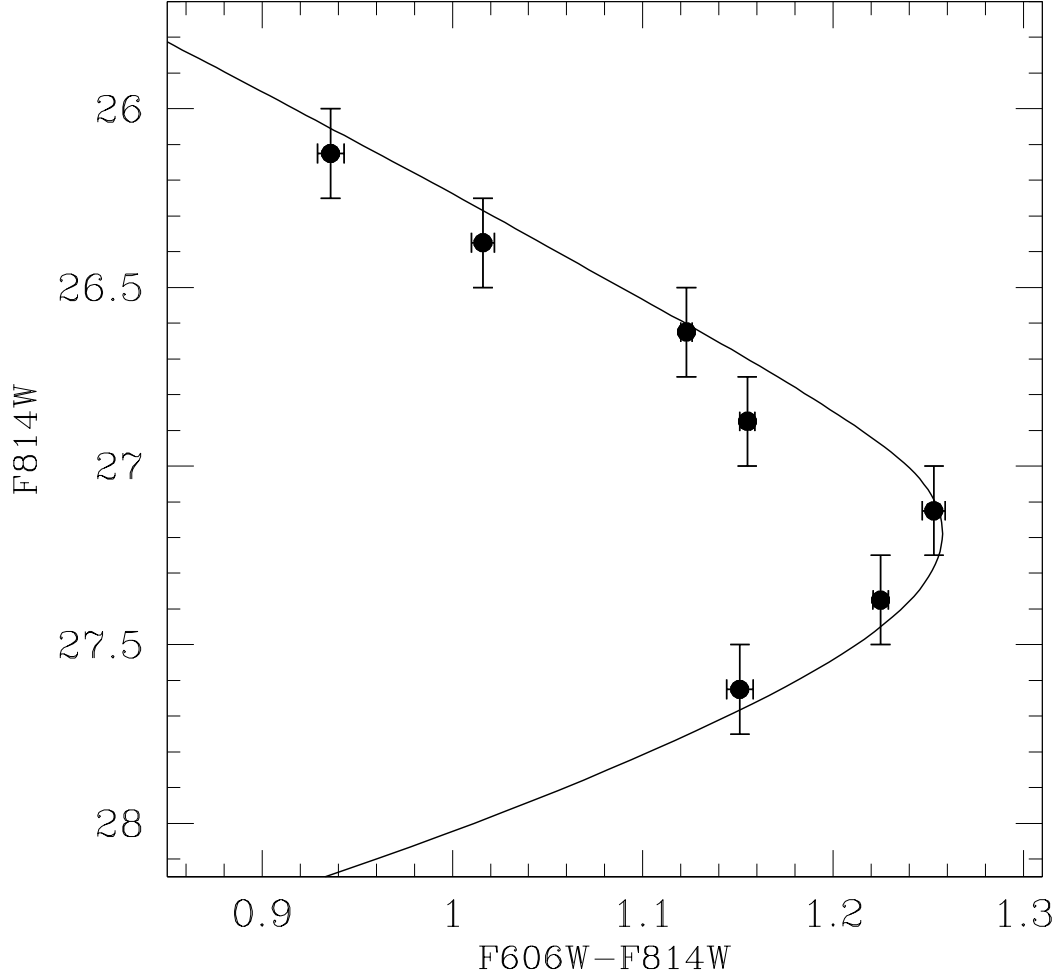


Fig. 6.— The large solid points are our empirical cooling sequence, as derived in the test. The solid line is the F606W-F814W/F814W cooling sequence for fixed radius from the models of Bergeron, suitably reddened and shifted, for a $0.5M_{\odot}$ model. The reddening used here is $E(\text{F606W-F814W})=0.16$ and the vertical shift is $\mu_{\text{F814W}} = 12.3$.

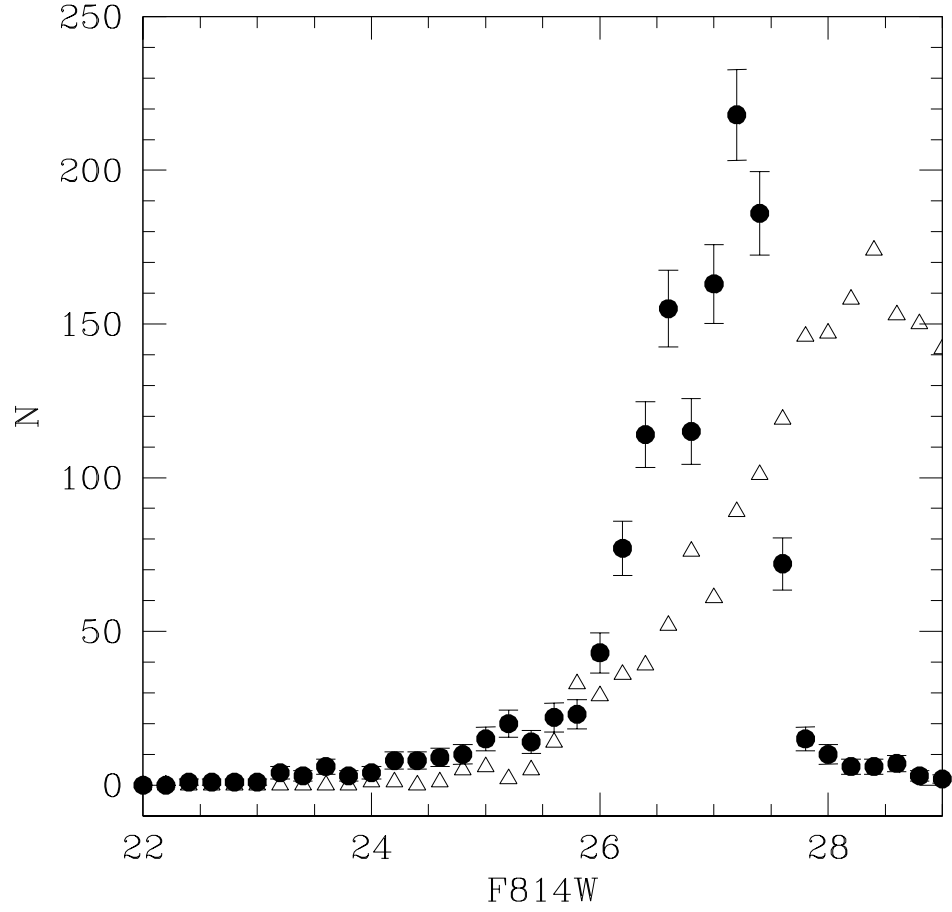


Fig. 7.— The solid points indicate the luminosity function of white dwarfs, identified by cuts of $|\text{CENXS}| < 0.02$ and $\text{ELONG} < 0.02$. The open triangles are the luminosity function of all objects bluer than the WDCS. The smoothly rising luminosity of these (mostly) galaxies argues strongly that the observed truncation in the luminosity function is real.

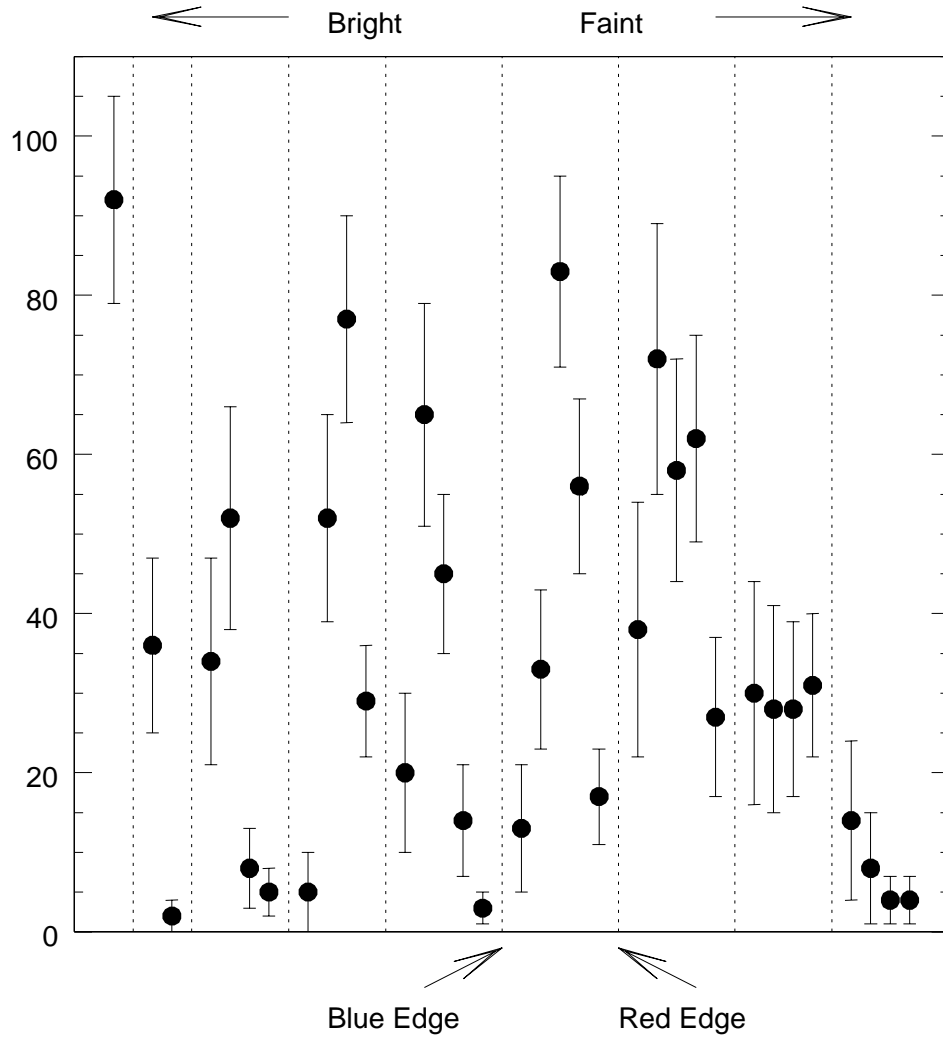


Fig. 8.— The bins indicate the sources counted in the colour-magnitude bins shown in Figure 4. The dotted lines delineate magnitude bins, with the magnitude increasing as one moves from the left to the right. Between a given pair of dotted lines, the binning indicates colour variation at fixed magnitude, with the colour getting redder from the left to the right. It is to this data that we compare our models.

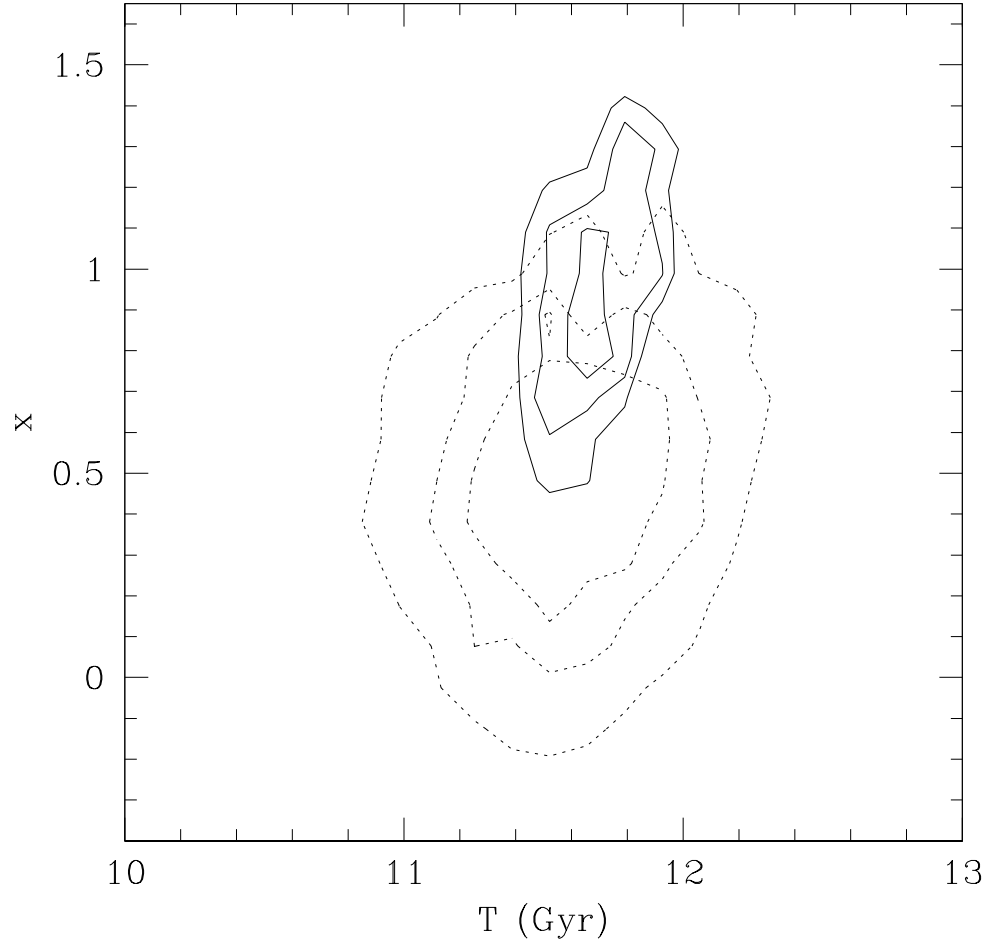


Fig. 9.— The solid contours are the 1, 2 and 3 σ contours for the Hess diagram fit to the model. The dotted contours correspond to the same confidence intervals, but now with the fit applied to the F814W luminosity function.

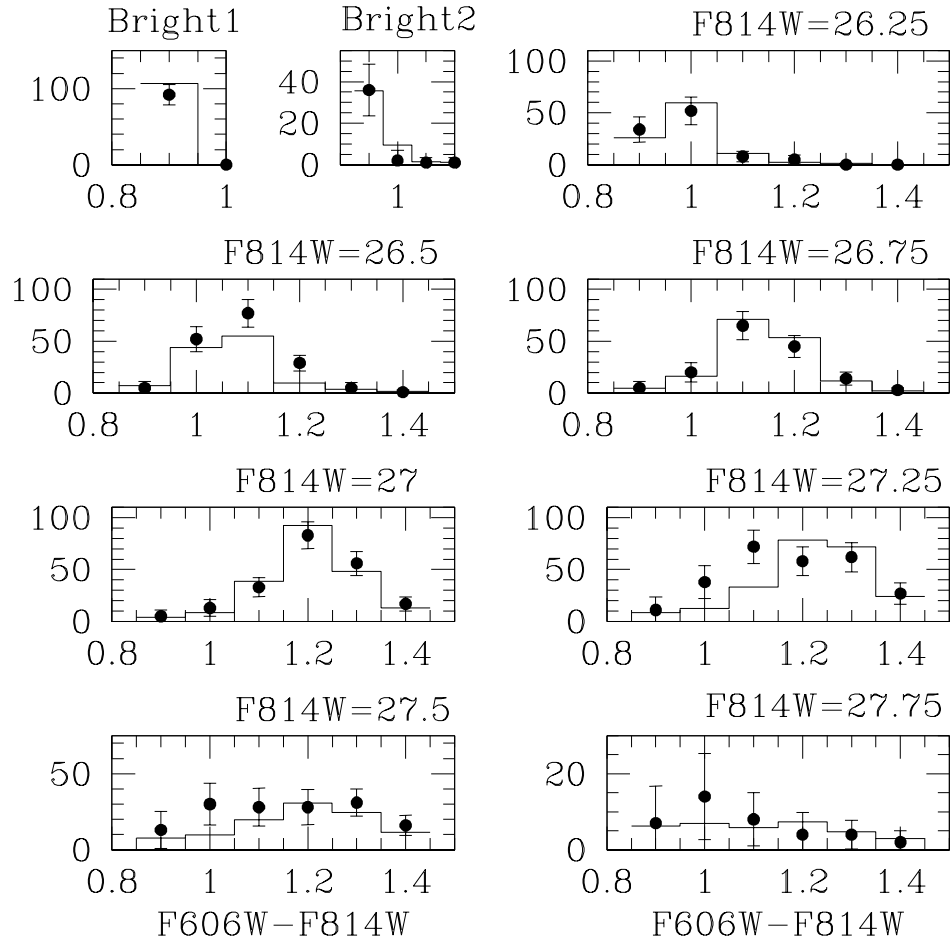


Fig. 10.— This model is an excellent fit overall. The models follow the observations both in colour trends at fixed magnitude as well as relative amplitudes as a function of magnitude. The one real discrepancy that remains is that the the model colour distribution at $F814W = 27.25$ is too red.

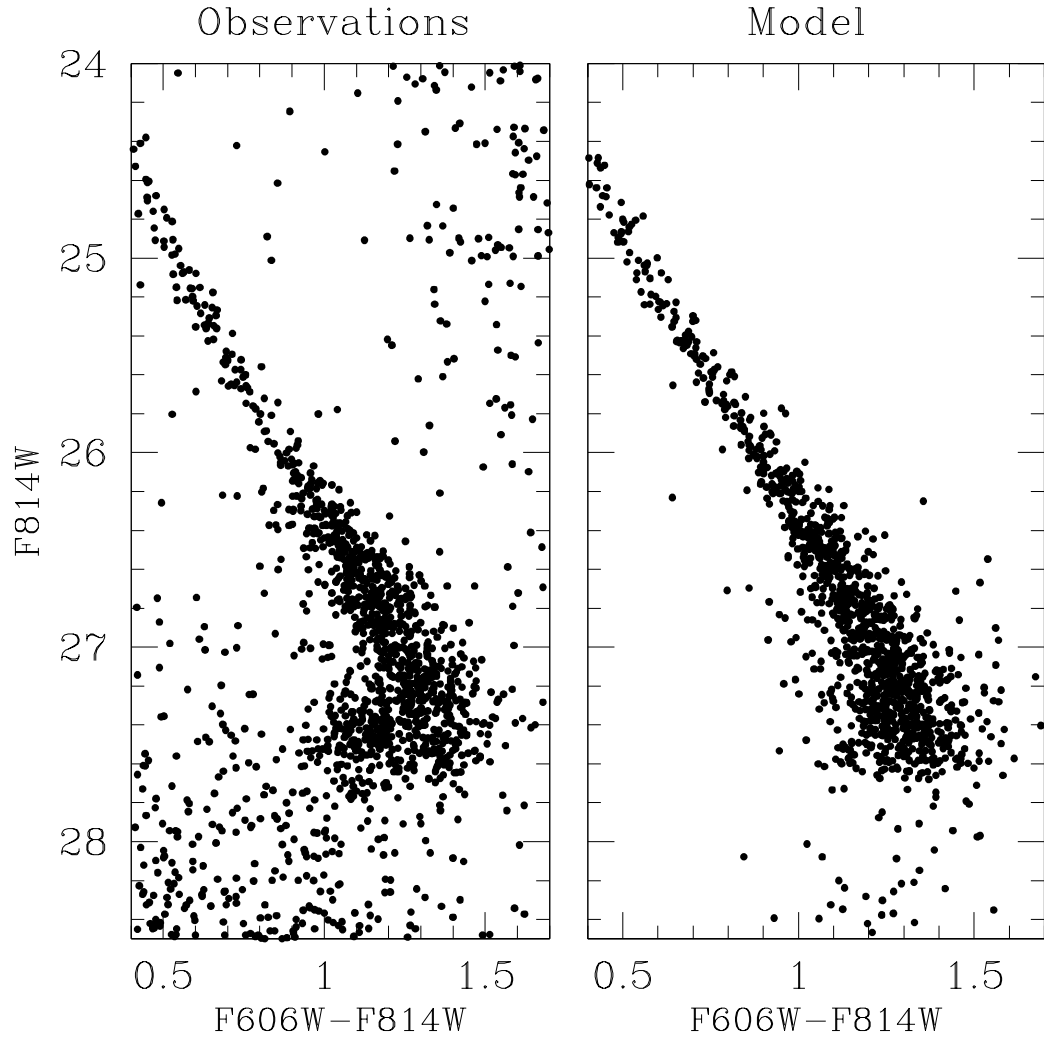


Fig. 11.— The left-hand panel shows the observed cooling sequence, after removal of the majority of background galaxies using CENXS cuts. The the right-hand panel shows a monte-carlo realisation of the simulated cooling sequence, adopting the best-fit age of 11.51 Gyr, and modeling the photometric scatter in accordance with the artificial star tests.

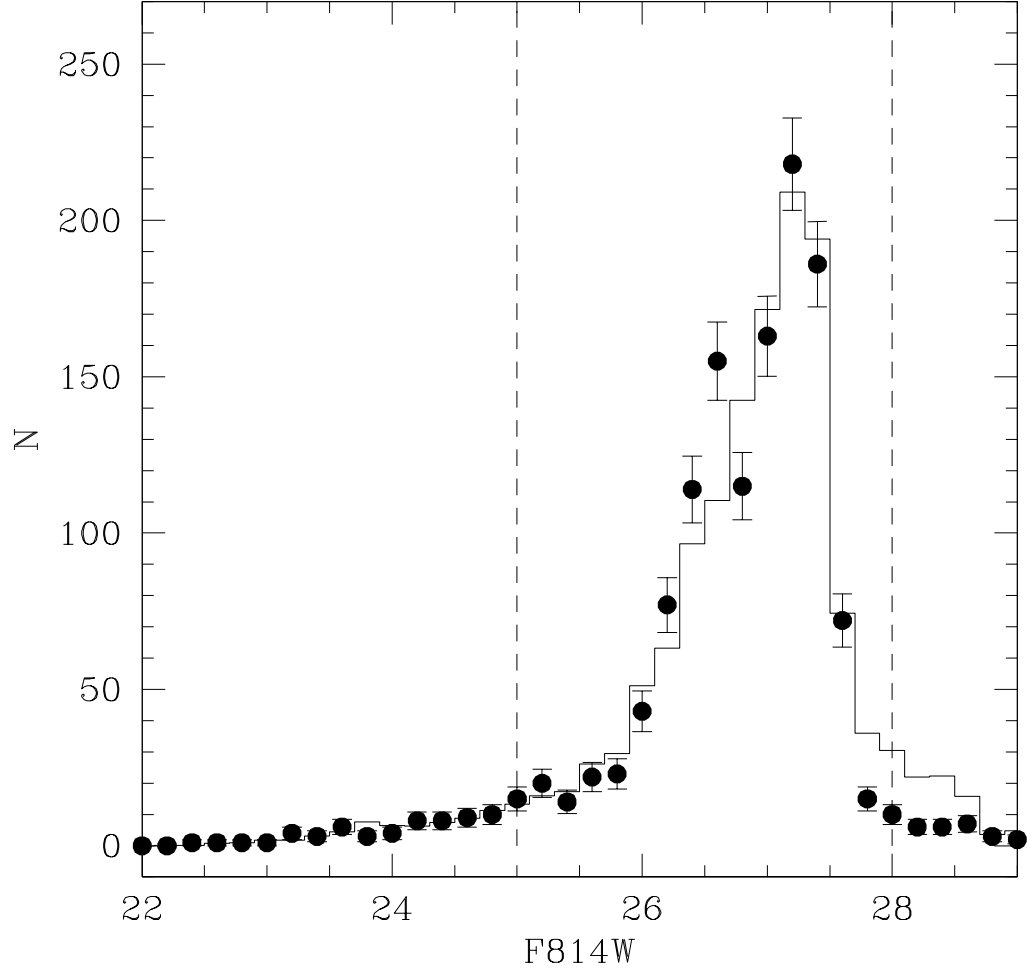


Fig. 12.— The solid points are the observed luminosity function. The solid histogram shows the model population, which includes both model white dwarfs and our estimate of the residual galaxy contamination per bin. The fitting region is delineated by the vertical dashed lines.

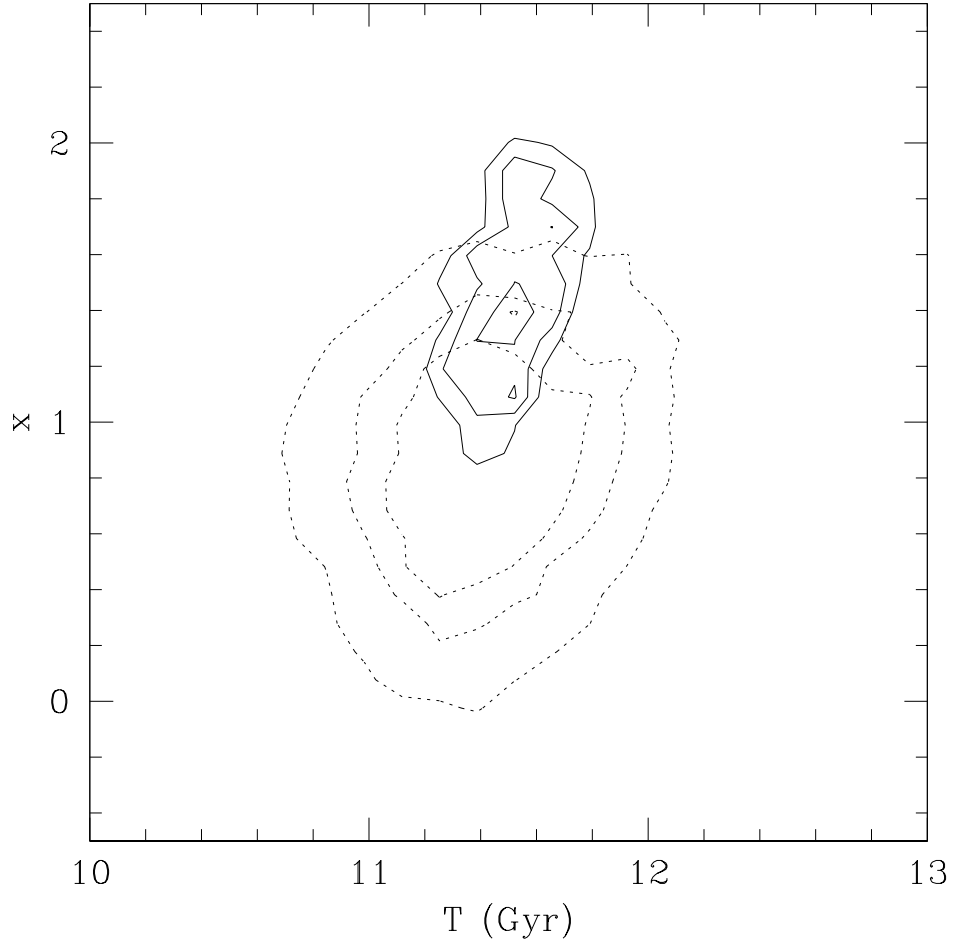


Fig. 13.— The solid contours are the confidence intervals for the Hess diagram fit but now using the $[Fe/H] = -2$ models from Dotter & Chaboyer. The dotted contours indicate the same but using the luminosity function.

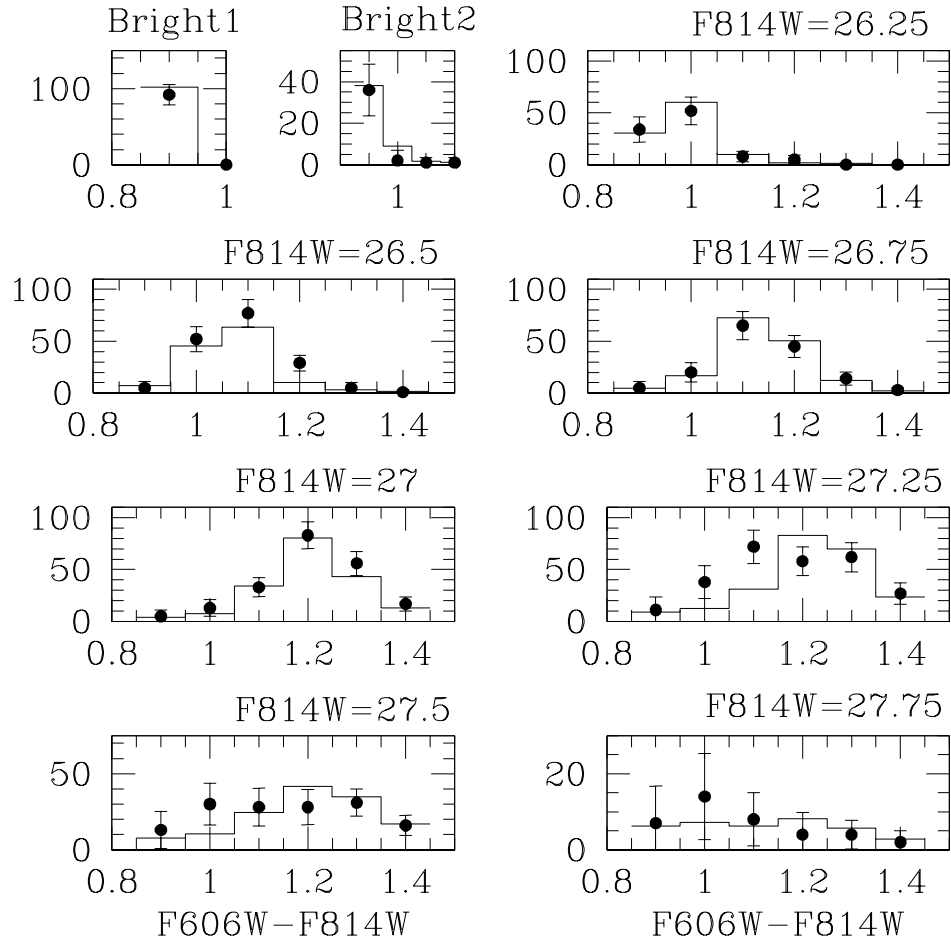


Fig. 14.— The histogram is once again the model fit to the observed distribution of white dwarfs in colour-magnitude space (solid points), this time for metal-poor progenitors and an age of 11.51 Gyr.

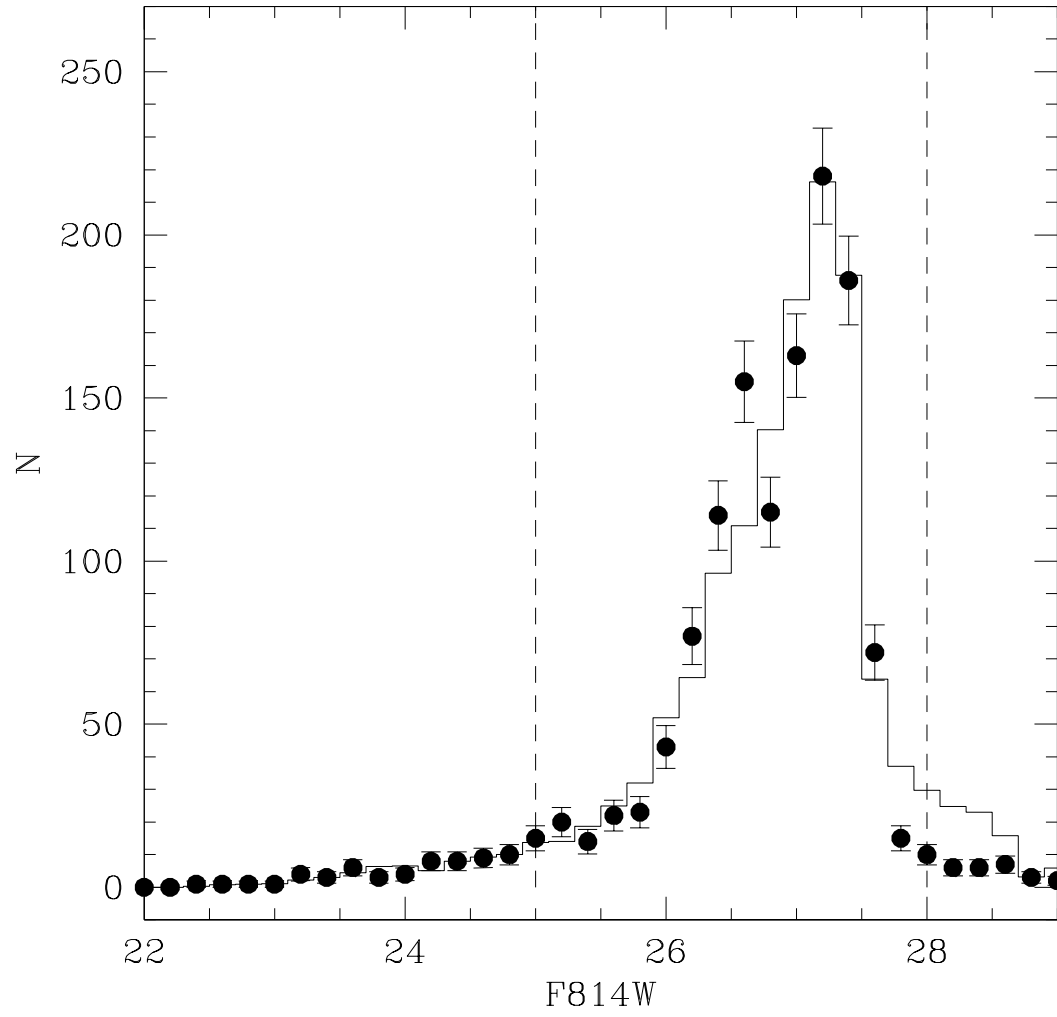


Fig. 15.— The model luminosity function shown is for an age of 11.46 Gyr.

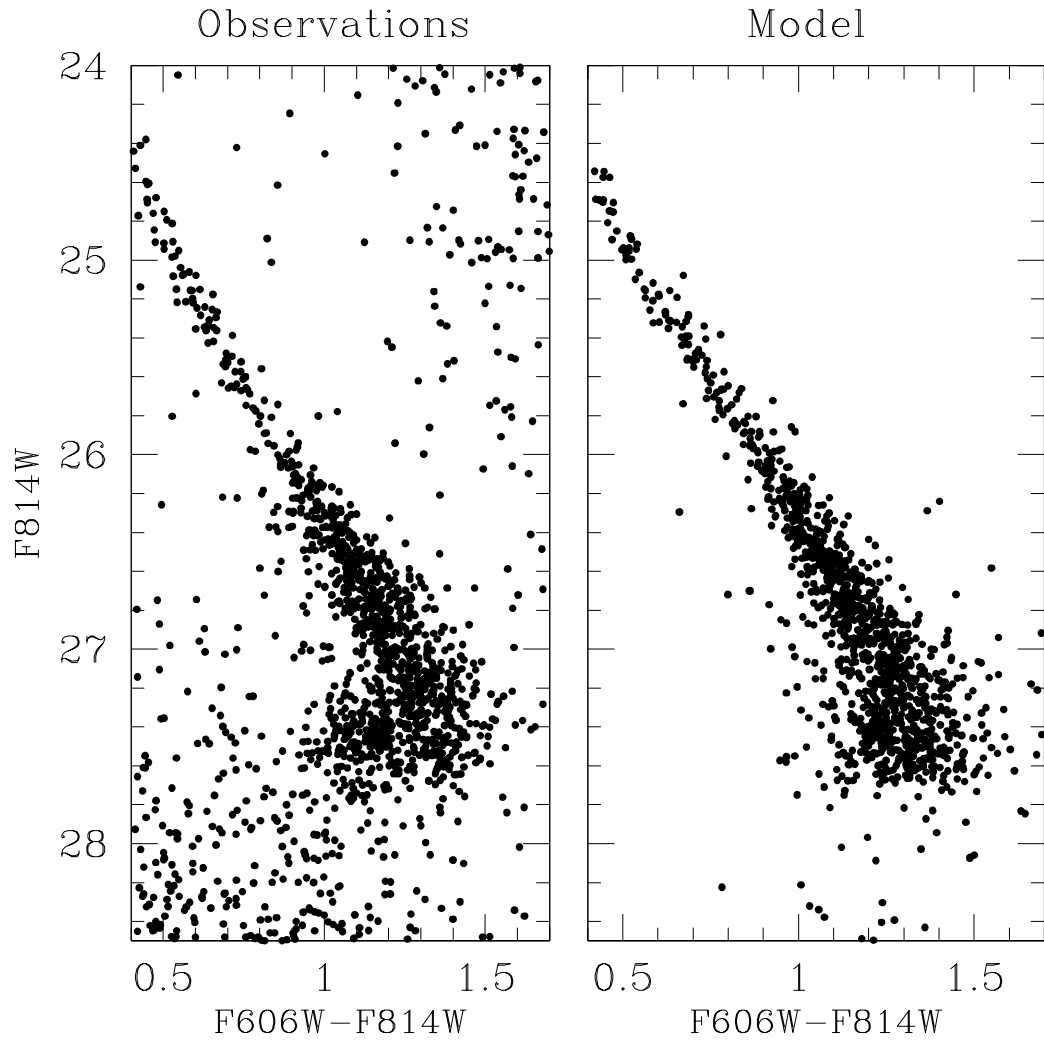


Fig. 16.— The left-hand panel is the observed cooling sequence while the right-hand side is a realisation of an 11.51 Gyr old model with metal-poor progenitors.

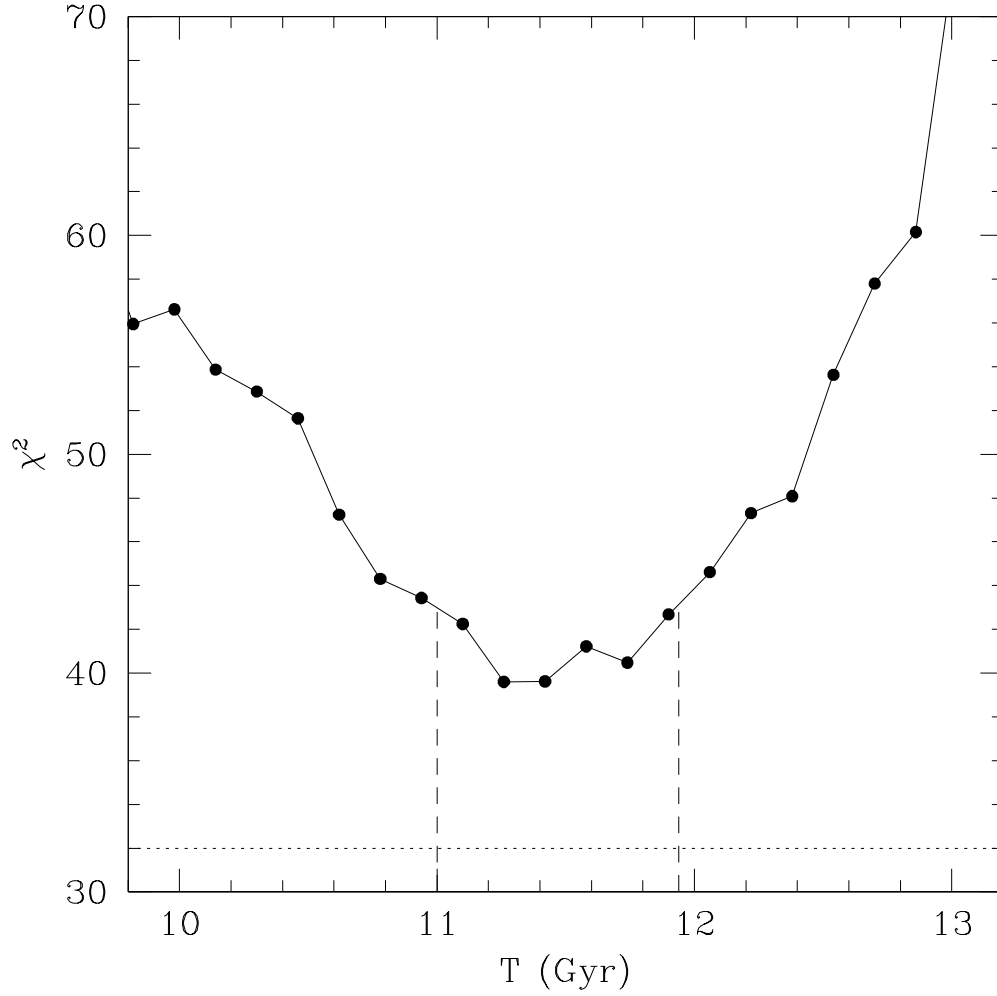


Fig. 17.— The χ^2 curve versus cluster age, marginalised over all other parameters for the metal-poor main sequence models (both those of Dotter & Chaboyer and those of Hurley et al). The dashed lines indicate the 2σ age range and the horizontal dotted line corresponds to $\chi^2 = 1$ per degree of freedom.

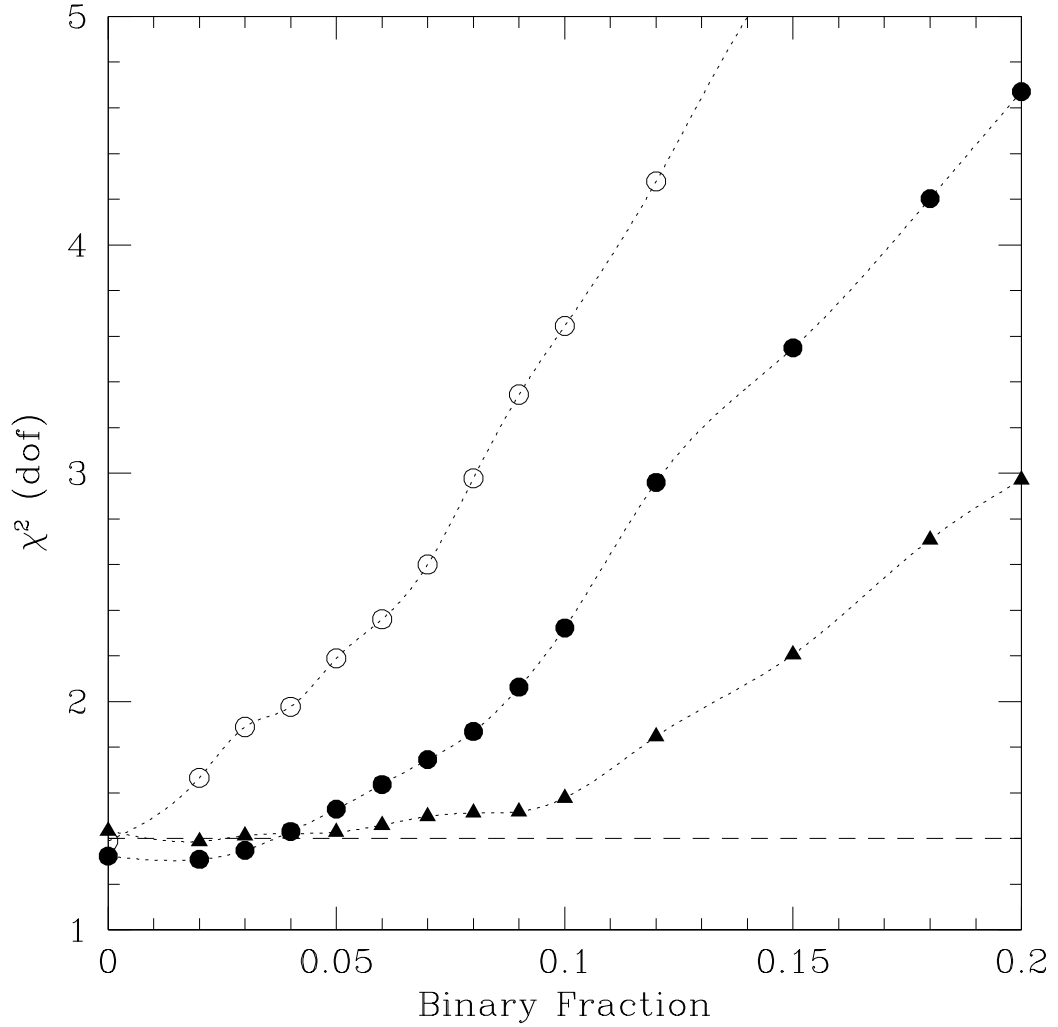


Fig. 18.— The open circles are the χ^2 per degree of freedom for fits to the observed F814W luminosity function, as a function of white dwarf binary fraction. The filled circles indicate fits to the Hess diagram - triangles in the case of our normal grid, and circles in the case of the expanded grid. The dashed line indicates the χ^2 (dof) limit on the expanded Hess fit.

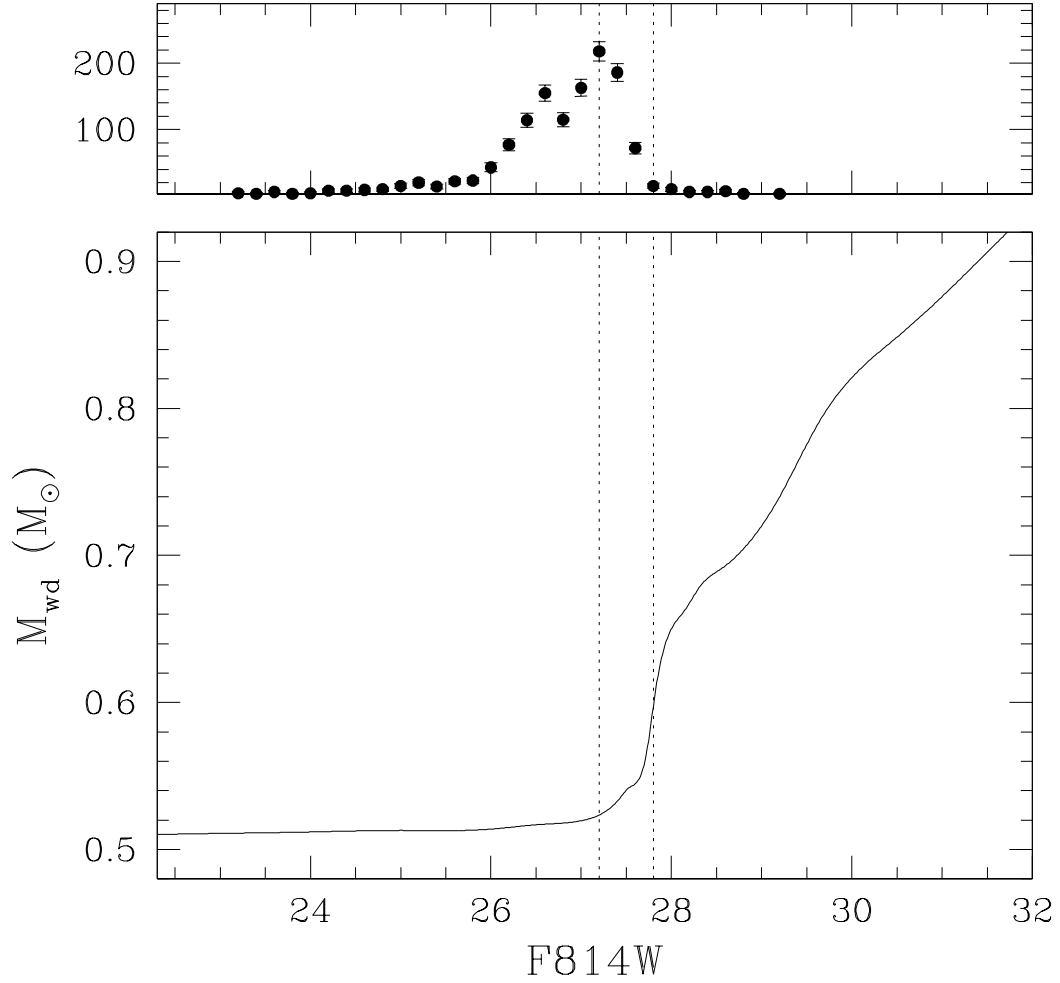


Fig. 19.— The upper panel shows our observed luminosity function, while the lower panel shows the relationship between white dwarf mass and F814W magnitude in our best-fit model. We see that the bulk of the luminosity function contains white dwarfs of the same mass and that the model masses only start to increase significantly as we reach the truncation of the luminosity function. In fact, it is the faster cooling of more massive white dwarfs at late times that causes this truncation. Note that this is at odds with the common interpretation of such a feature as being due to the faintest white dwarfs that exist in the cluster.

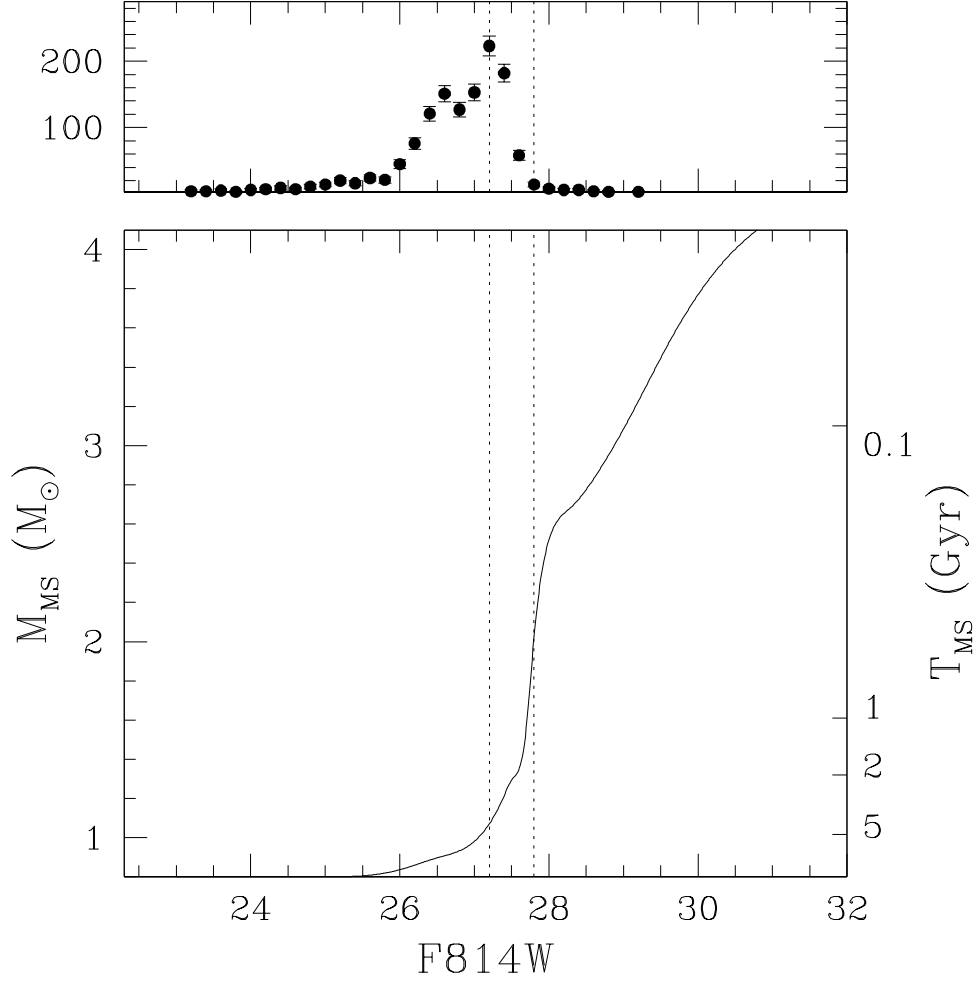


Fig. 20.— This figure is similar to Figure 19 expect we now show the main sequence mass of the white dwarf progenitors in the best fit model. We see that the white dwarf luminosity function probes only a rather limited range in stellar masses.

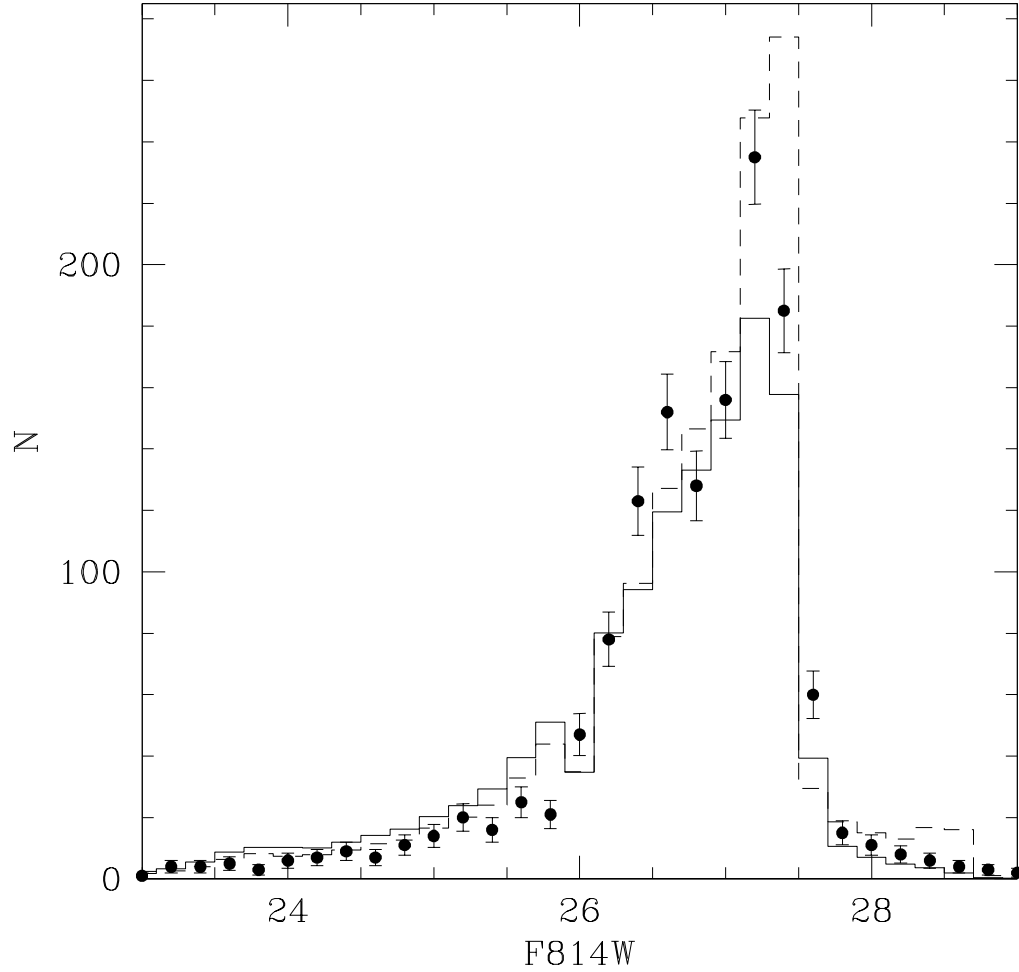


Fig. 21.— This figure demonstrates that the luminosity function truncation is a real feature of the white dwarf population and not simply a function of observational incompleteness. The solid histogram is the best-fit model to the observed luminosity function and the dashed histogram is the very same model but now without taking into account the loss of stars due to incompleteness. We see that the sharp peak is slightly smoothed out by the loss of stars due to crowding, but that the sharp truncation is still preserved.

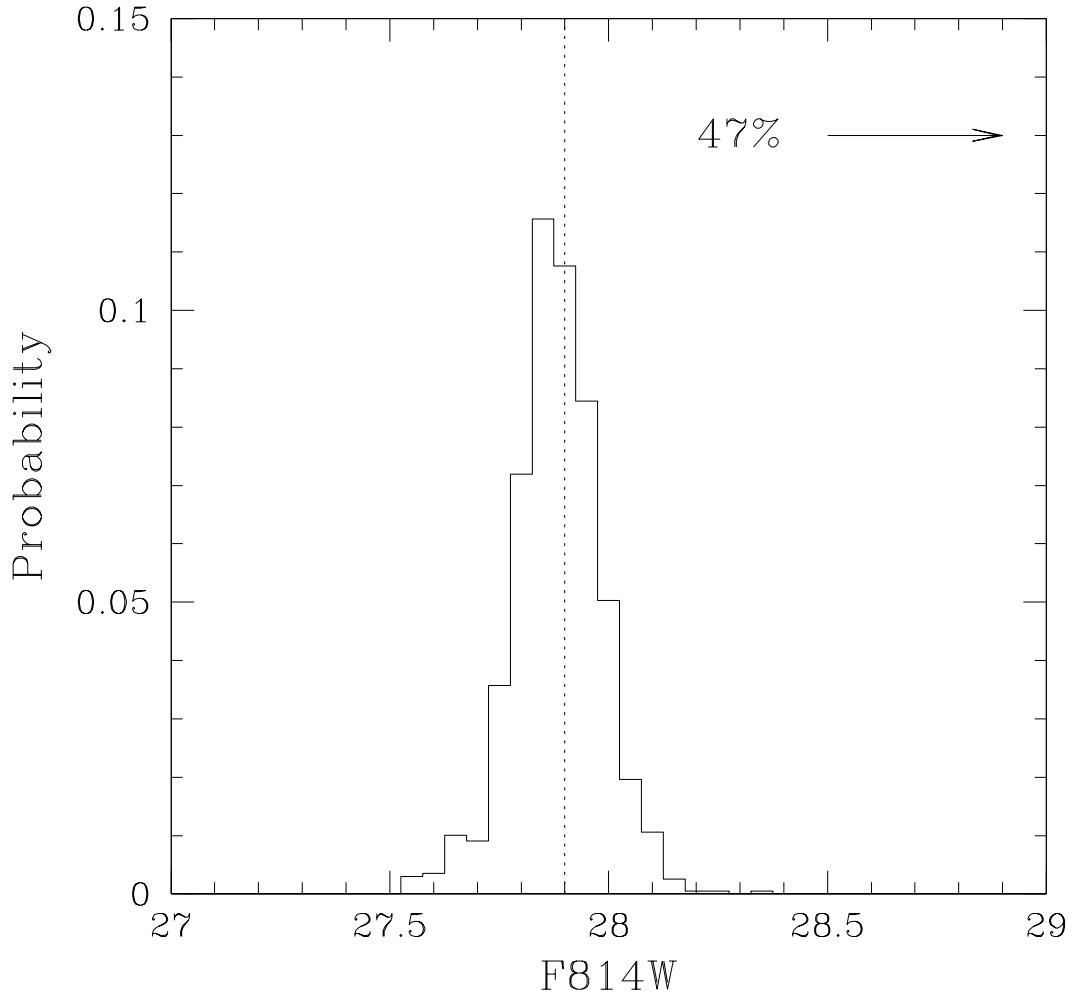


Fig. 22.— This figure illustrates the nature of our observational incompleteness, as determined by artificial star tests. The dotted line indicates the input magnitude (chosen to represent the end of the luminosity function) and the solid histogram indicates the spread in magnitude of those artificial stars successfully recovered. Note that this population represents only 53% of the input stars. The others are never recovered because they are located too close to much brighter stars.

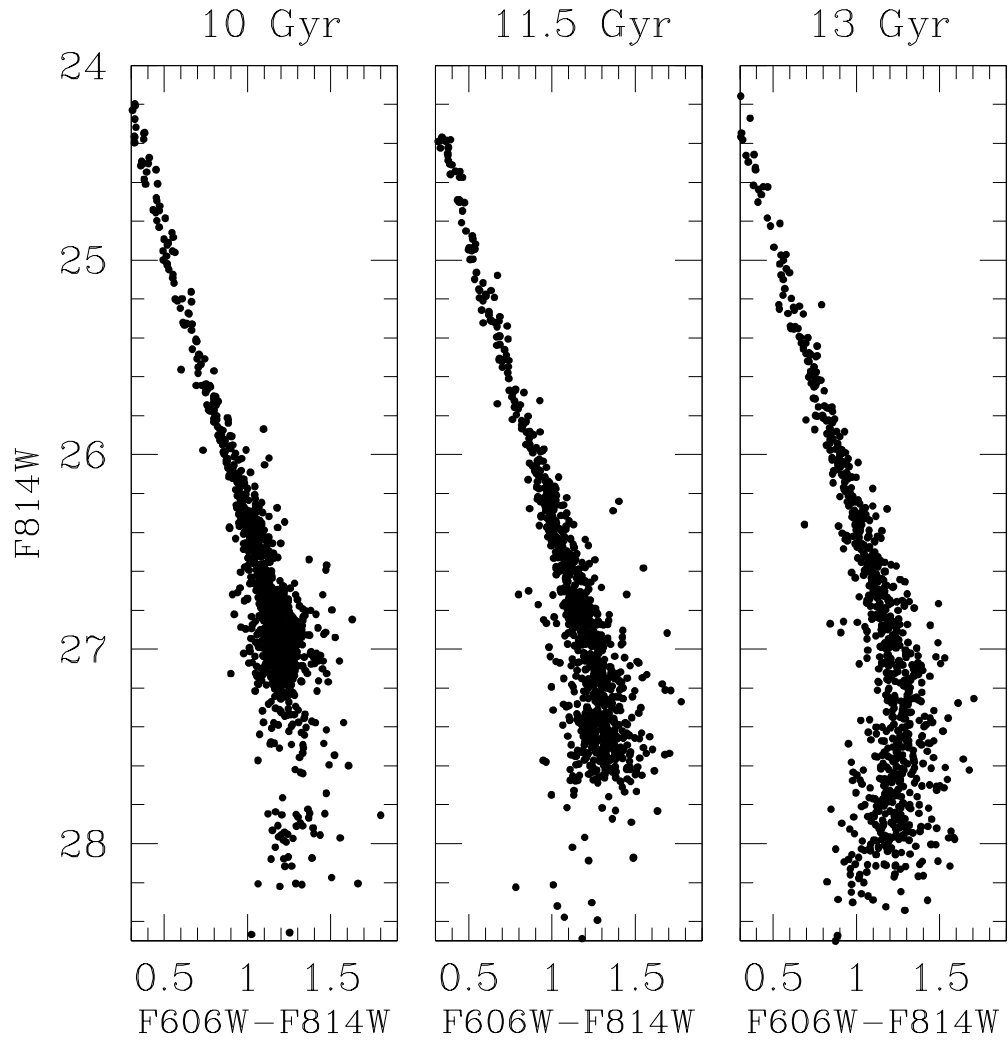


Fig. 23.— The models in all three panels are identical except for the assumed age. The center panel has an age of 11.5 Gyr and corresponds to our best-fit model for NGC 6397. The left hand panel shows a younger population, with age of 10 Gyr, and the right hand panel shows an older one, with age 13 Gyr. It is clear from a simple visual inspection that neither of the side panels are a good match to the observed population seen in Figure 11 or 16.

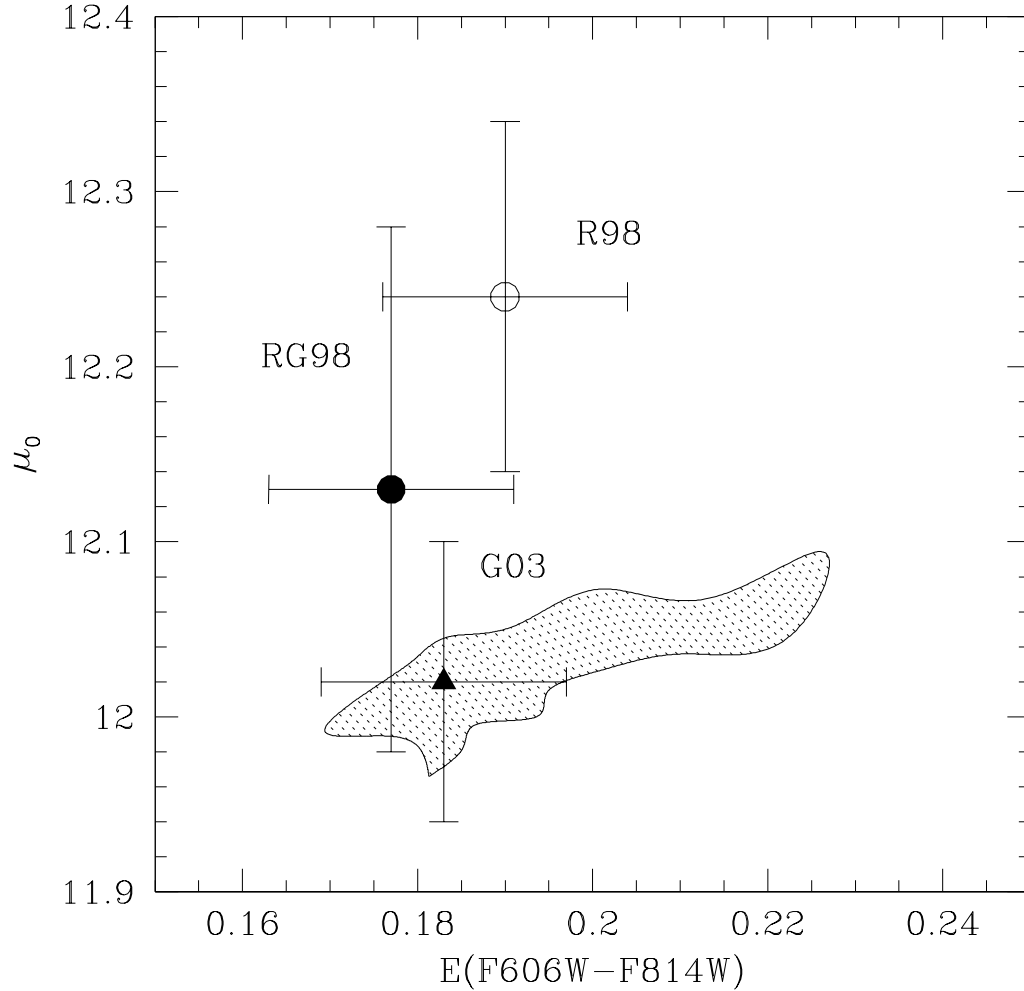


Fig. 24.— The shaded region is the 2σ age range for distance and reddening allowed by fitting to the white dwarf cooling sequence. The solid point with the error bar represents the distance inferred by Reid & Gizis (1998), plotted at their assumed reddening. Similarly, the inferred values from Reid (1998) and Gratton et al (2003) are also shown. The reddenings have been converted from the ground-based colours to the ACS photometric system using the prescription of Sirianni et al (2005). The horizontal error bars represent the effect of assuming different underlying spectral types, spanning M5 to O2, when converting from ground-based to HST magnitudes.

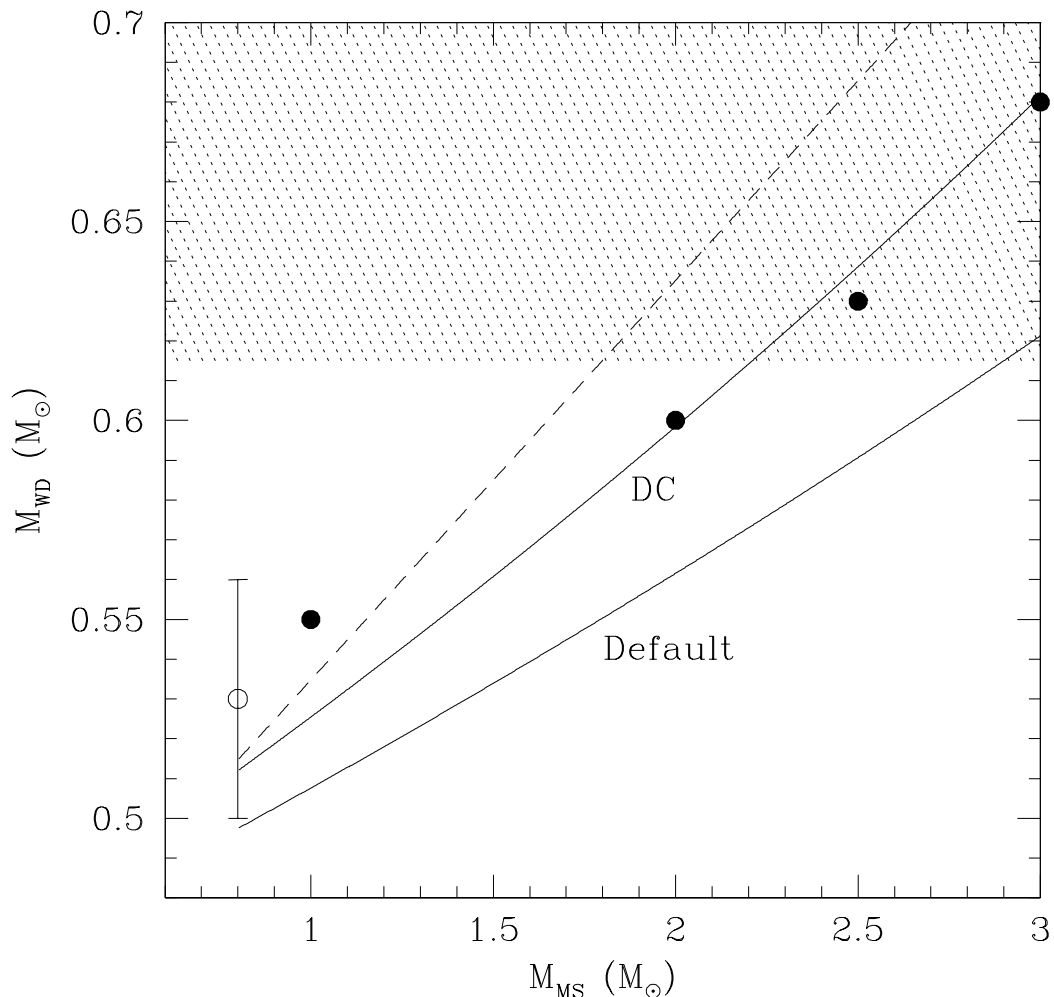


Fig. 25.— The solid lines indicate our best fit initial-final mass relations for the default models and for the metal-poor models with Dotter & Chaboyer main sequence lifetimes. The solid points are the empirical relation inferred by Weidemann (2000) and the dashed line indicates the best-fit linear relation espoused by Ferrario et al (2005). The open circle, with the error bar, is the mean upper cooling sequence mass inferred by Moehler et al (2004). Our fit is only constrained for a limited range of white dwarf masses (see Figure 19) and so we shade the range of white dwarf masses that fall beyond our magnitude limit. We see that our best-fit models overall (the DC models) are in excellent agreement with Weidemann’s empirical determination.

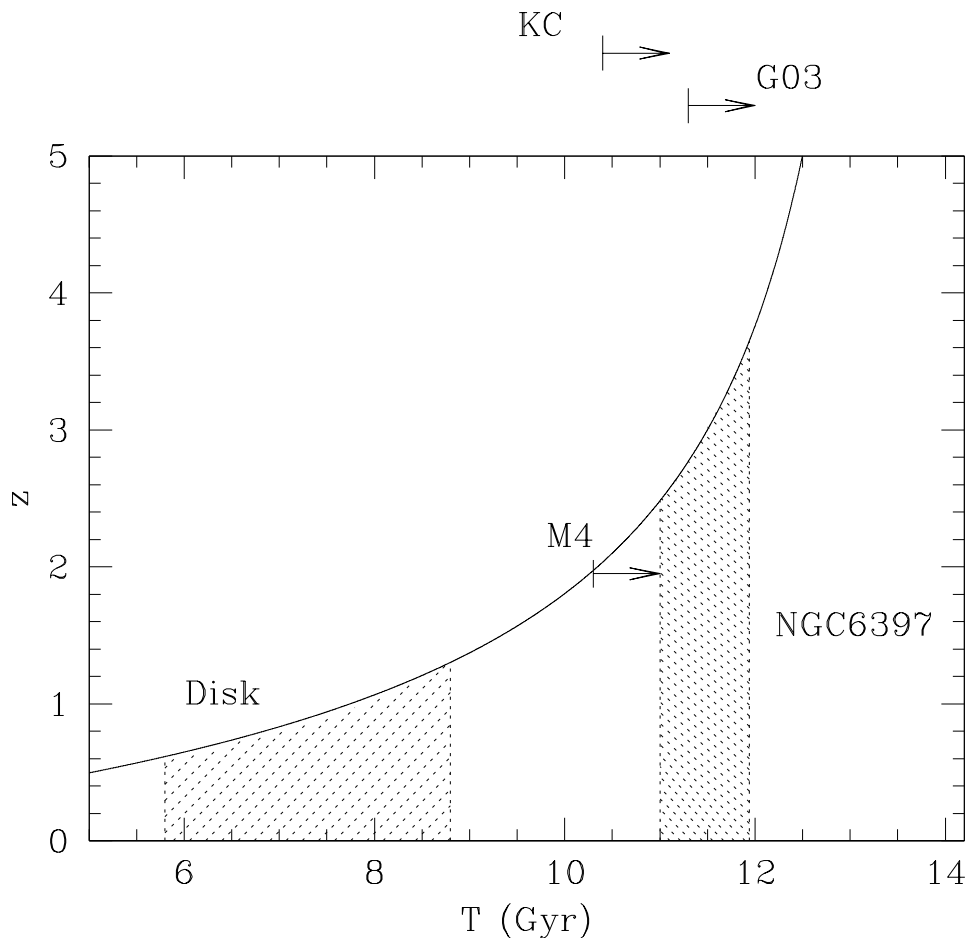


Fig. 26.— The solid curve indicates the relationship between cosmological redshift z and lookback time for the best-fit flat universe model from Spergel et al (2003). The shaded regions indicate white dwarf cooling ages (2σ range) for the Galactic disk (Hansen et al 2002) and NGC 6397 (this paper) and the arrow indicates the lower limit on the age for M4 (Hansen et al 2004). Above the plot we show two 95% lower limits. The limit marked KC indicates the lower limit for the age of the globular cluster system as whole, taken from Krauss & Chaboyer (2003). The limit marked G03 is the 2σ lower limit on the age of NGC6397, based on the results of Gratton et al (2003). The comparison indicates that our age determination is consistent with, but also more accurate than, the best measurements using the MSTO method.

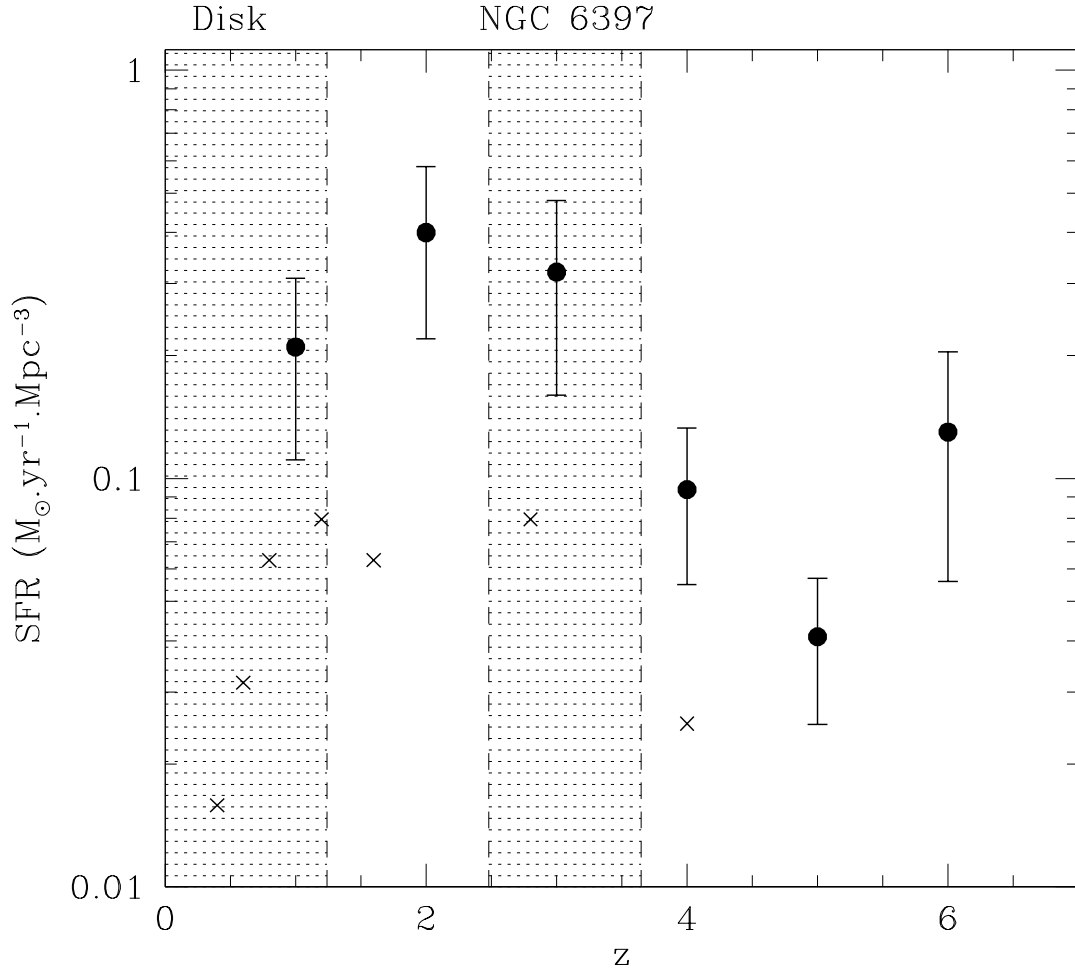


Fig. 27.— The solid points represent the Hubble Ultra-Deep Field star formation rates (corrected for extinction and surface brightness) measured by Thompson et al (2006). The crosses are the extinction corrected values measured from the Hubble Deep Field by Madau et al (1996). The shaded regions indicate the epoch in which the Galactic Disk and NGC 6397 formed, according to our measures of the white dwarf cooling.

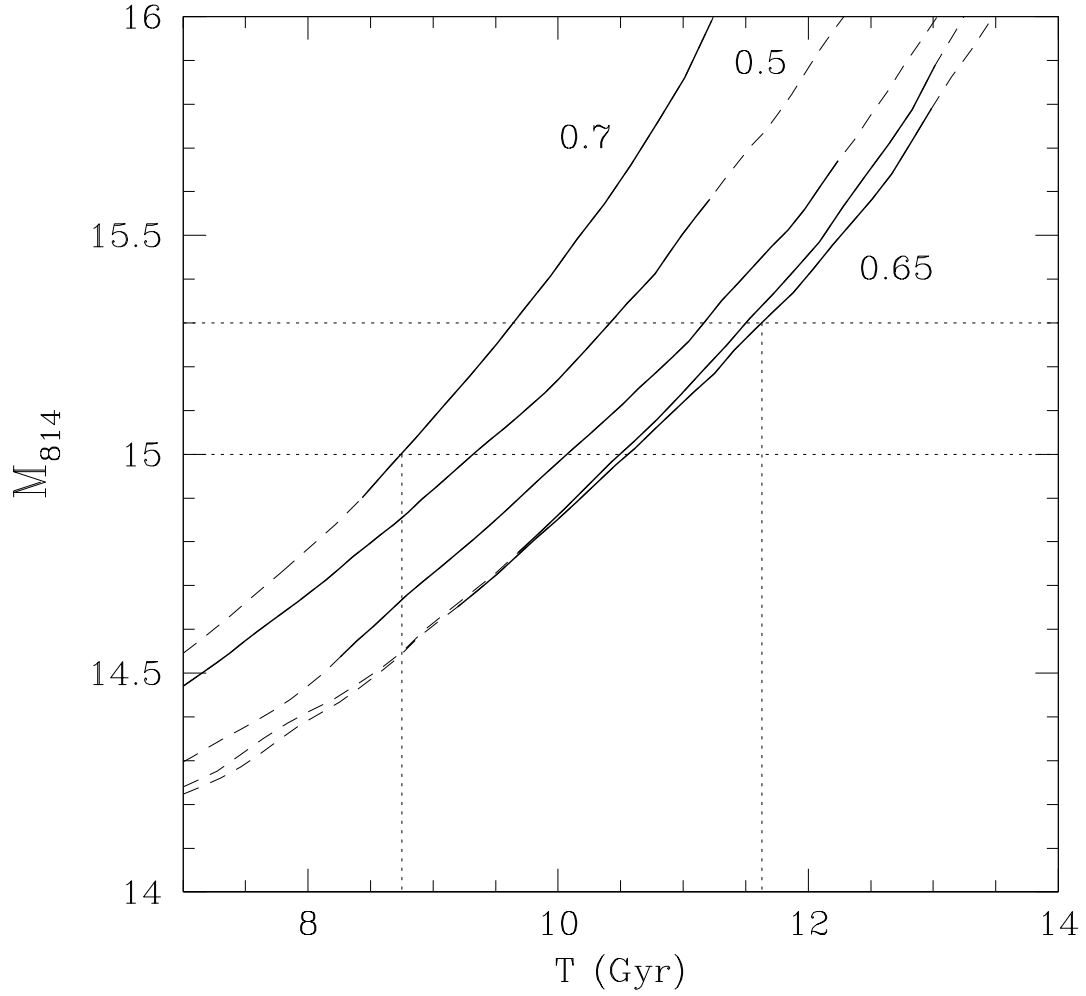


Fig. 28.— The horizontal dotted lines indicate the inferred absolute magnitude range where the truncation in the cooling sequence occurs. The various curves show the results for cooling models of different masses (except for the leftmost curve, labelled $0.7M_{\odot}$, the mass increases from left to right, in increments of $0.05M_{\odot}$, from that labelled $0.5M_{\odot}$ to that labelled $0.65M_{\odot}$). Those parts of each curve that are solid correspond to F606W-F814W colours consistent with those at the observed truncation, while the dashed parts do not. The vertical dotted lines indicate the inferred age range.

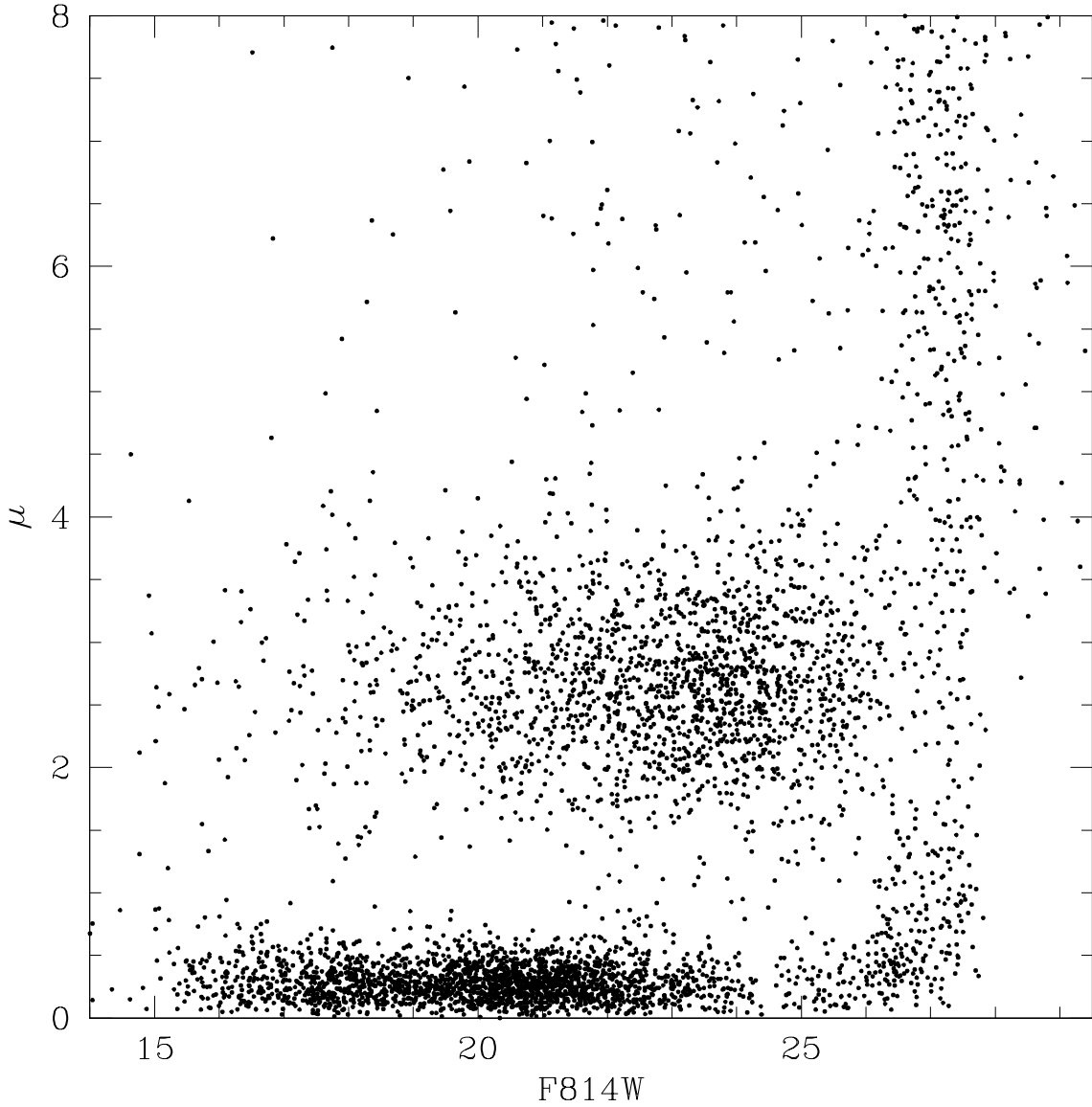


Fig. 29.— The proper motion displacements of all detected point sources that overlap with WFPC2 data, as a function of F814W. We can see the excellent separation for bright magnitudes, failing at $F814W \sim 26.5$. Brighter than this magnitude, the stars separate cleanly into cluster members ($\mu \sim 0$) and background stars ($\mu \sim 2.5$). Fainter than this magnitude, most real stars in the ACS data are matched to noise peaks in the WFPC2 data, resulting in large spurious displacements.

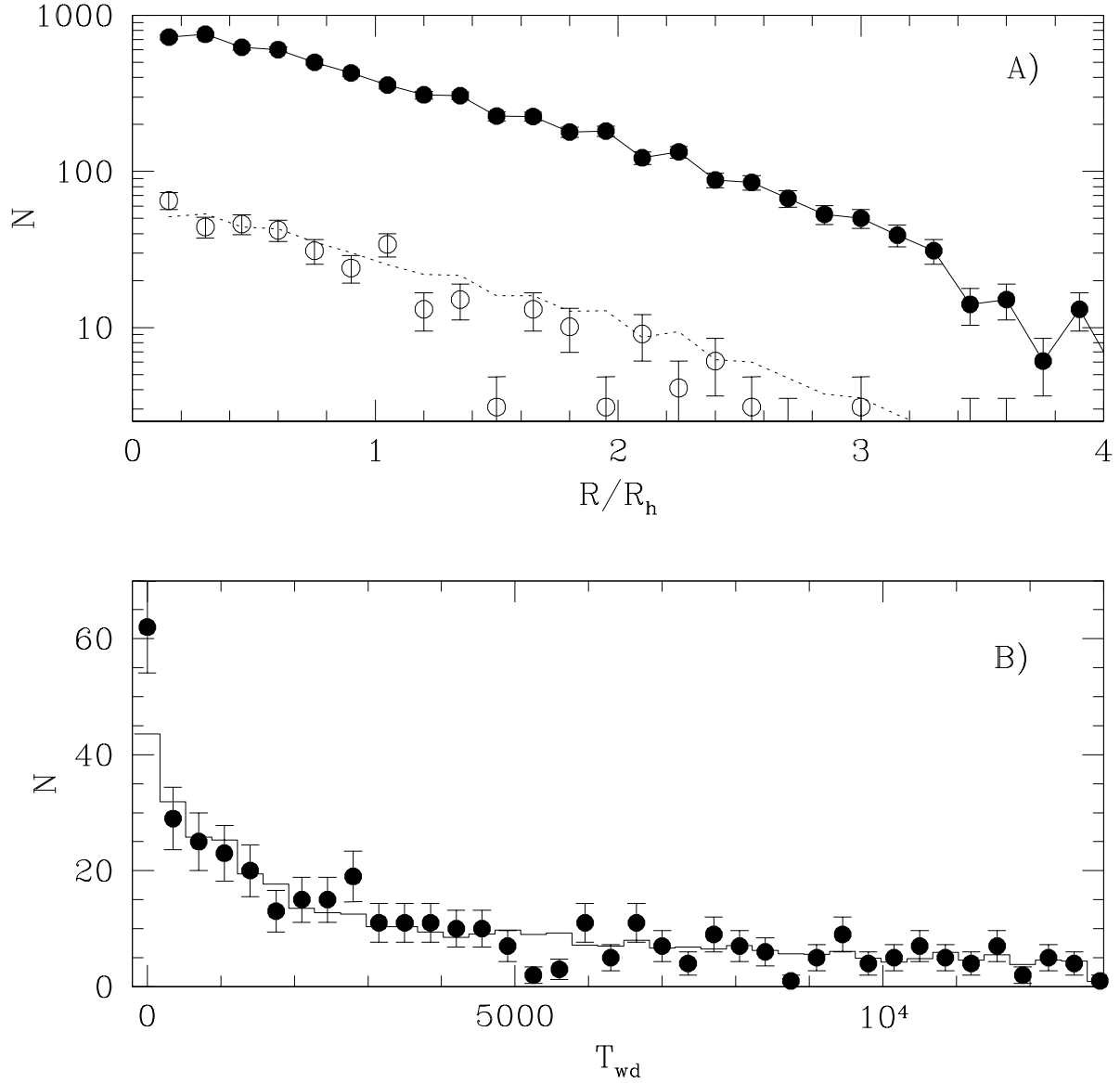


Fig. 30.— A) The filled circles and solid line indicate the radial profile of ‘bachelor’ white dwarfs – those which result from single star evolution and which experience no perturbations during the course of their evolution. The open circles represent the radial profile of ‘divorced’ white dwarfs, which represent stars which spent some fraction of their life in a binary but are now single. The dotted histogram is the same as the solid histogram, but scaled by a factor 0.07. The divorced white dwarfs follow the same radial profile as the bachelors. Radii are in units of the half-mass radius of the cluster. B) The filled circles show the distribution of divorced white dwarfs with T_{wd} – the time at which the white dwarf formed (i.e. $T_{wd} = 0$ corresponds to the birth of the cluster). The solid histogram represents the age distribution of the bachelor white dwarfs, once again suitably scaled. There is clearly little difference in the age distribution between the

two populations. Even if the deviation at $T_{\text{wd}} < 200$ Myr is real, it is too small to have any effect on our modeling.

Table 1. NGC 6397 White Dwarf Distribution

F814W	F606W-F814W					
	0.9–1.0	1.0–1.1	1.1–1.2	1.2–1.3	1.3–1.4	1.4–1.5
Bright Bin	92 (13)					
26.00–26.25	36 (11)	2 (2)				
26.25–26.50	34 (13)	52 (14)	8 (5)	5 (3)		
26.50–26.75	5 (5)	52 (13)	77 (13)	29 (7)		
26.75–27.00		20 (10)	65 (14)	45 (10)	14 (7)	3 (2)
27.00–27.25		13 (8)	33 (10)	83 (12)	56 (11)	17 (6)
27.25–27.50		38 (16)	72 (17)	58 (14)	62 (13)	27 (10)
27.50–27.75		30 (14)	28 (13)	28 (11)	31 (9)	
27.75–28.00		14 (10)	8 (7)	4 (3)	4 (3)	

Note. — Errors (statistical and systematic) in each bin are listed in parentheses.

Table 2. Empirical NGC 6397 White Dwarf Cooling Sequence

F814W	F606W-F814W	$\Delta(\text{F606W-F814W})$
26.0	0.936	0.007
26.25	1.016	0.006
26.5	1.123	0.003
26.75	1.155	0.004
27.0	1.253	0.006
27.25	1.225	0.004
27.5	1.151	0.007

Table 3. F814W Photometric Scatter

F814W	N_{in}	N_{out}	$\Delta F814W$																
			-0.40	-0.35	-0.30	-0.25	-0.20	-0.15	-0.10	-0.05	0.00	0.05	0.10	0.15	0.20	0.25	0.30	0.35	0.40
22.0	0	0	0	0	0	0	0	0	0	0	0	0	0	0	0	0	0	0	0
22.2	0	0	0	0	0	0	0	0	0	0	0	0	0	0	0	0	0	0	0
22.4	2750	2572	1	1	4	4	14	32	84	2333	83	5	1	1	2	1	0	0	0
22.6	2873	2684	3	0	3	4	11	14	55	2465	115	6	3	1	0	0	0	0	0
22.8	2917	2703	1	1	4	6	11	10	65	2487	101	5	3	0	0	1	0	0	0
23.0	2807	2610	0	1	4	4	6	8	31	2386	159	3	0	0	0	0	0	0	0
23.2	2781	2528	1	0	0	1	1	7	37	2239	230	8	3	0	0	0	0	0	0
23.4	2781	2525	0	0	3	2	2	4	21	2222	253	14	1	1	0	0	0	0	0
23.6	2866	2572	0	0	0	0	1	4	24	2205	316	18	3	0	0	0	0	0	0
23.8	2919	2631	0	0	0	1	1	3	12	2221	364	21	4	1	0	0	0	0	0
24.0	2805	2485	0	0	0	1	1	5	25	2035	390	20	5	0	0	0	0	0	1
24.2	2782	2446	0	0	0	0	1	4	38	1901	458	33	6	0	0	0	0	1	0
24.4	2774	2403	0	0	0	1	1	6	28	1839	477	34	9	4	0	0	0	0	0
24.6	2870	2460	1	0	1	2	5	4	32	1813	540	44	15	0	1	1	0	0	0
24.8	2915	2504	0	0	1	2	1	6	36	1763	628	51	9	3	1	0	0	0	0
25.0	2808	2349	0	0	0	1	1	5	46	1620	595	61	14	1	0	0	0	0	0
25.2	2784	2332	0	0	0	1	1	6	70	1436	707	81	20	3	1	0	0	0	0
25.4	2774	2249	0	0	0	0	2	8	55	1324	750	73	24	8	1	0	1	0	0
25.6	2879	2331	0	1	0	1	3	17	83	1325	783	84	19	9	2	0	0	0	0
25.8	2910	2322	0	1	0	3	3	21	74	1229	840	96	34	12	2	0	0	0	0
26.0	2806	2190	0	0	0	2	8	25	84	1087	815	108	36	13	5	1	0	1	0
26.2	2787	2112	1	2	3	3	7	21	89	988	814	130	35	8	1	0	0	0	0
26.4	2773	2042	0	1	3	2	10	20	116	884	785	139	43	19	12	1	1	0	0
26.6	2880	2075	1	0	4	4	12	36	169	803	792	169	59	8	7	2	0	0	0
26.8	2911	2041	1	0	5	7	21	39	163	762	720	232	53	21	10	2	0	0	0
27.0	2804	1888	0	0	3	9	21	46	185	629	631	230	79	33	14	3	1	0	0

Table 3—Continued

F814W	N_{in}	N_{out}	$\Delta F814W$																
			-0.40	-0.35	-0.30	-0.25	-0.20	-0.15	-0.10	-0.05	0.00	0.05	0.10	0.15	0.20	0.25	0.30	0.35	0.40
27.2	2785	1751	0	2	3	9	27	55	202	530	515	254	92	30	18	4	4	2	0
27.4	2780	1665	0	1	5	10	21	77	216	418	448	271	112	47	20	7	5	1	0
27.6	2882	1636	1	3	7	15	35	95	233	370	381	263	128	60	26	9	4	2	1
27.8	2912	1541	1	7	7	22	38	99	209	311	315	244	154	65	41	12	2	6	2
28.0	2796	1350	1	2	12	16	54	106	172	234	251	186	143	77	46	22	12	4	4
28.2	2786	1178	2	12	15	27	58	97	157	170	191	148	119	85	37	21	5	10	4
28.4	2781	937	8	12	22	28	40	97	102	149	119	112	77	69	46	24	9	8	4
28.6	2882	718	7	14	23	31	53	75	91	85	73	80	63	41	21	15	10	5	6
28.8	2915	376	3	11	28	26	32	34	36	41	33	31	22	18	14	11	3	1	2
29.0	2790	222	10	14	20	14	28	17	19	14	21	10	13	4	6	0	3	0	1
29.2	2783	130	2	10	14	12	10	17	8	10	5	4	1	2	1	1	3	0	1
29.4	2783	53	3	5	1	4	7	2	0	1	3	0	3	2	0	0	1	1	0
29.6	2877	37	2	2	2	2	1	1	2	0	1	0	0	0	0	0	0	0	0

Note. — Each bin corresponds to the difference between recovered magnitude and input magnitude. Thus, a negative value implies that those stars were recovered as being brighter than their true magnitudes.

Table 4. F606W Photometric Scatter

F606W	N_{in}	N_{out}	$\Delta F606W$																
			-0.40	-0.35	-0.30	-0.25	-0.20	-0.15	-0.10	-0.05	0.00	0.05	0.10	0.15	0.20	0.25	0.30	0.35	0.40
22.0	0	0	0	0	0	0	0	0	0	0	0	0	0	0	0	0	0	0	0
22.2	835	785	0	0	0	0	0	3	19	743	16	1	0	0	0	0	0	0	0
22.4	2533	2360	0	0	0	2	0	9	35	2238	72	2	1	0	0	0	0	0	0
22.6	2624	2440	0	0	1	1	0	4	29	2236	161	4	0	0	0	1	0	1	0
22.8	2599	2405	0	0	0	0	3	4	26	2081	277	1	1	1	0	0	0	0	0
23.0	2552	2366	0	2	1	0	1	3	11	1933	402	4	0	0	1	0	0	1	0
23.2	2523	2310	0	0	0	1	0	3	11	1772	520	1	0	0	0	0	0	0	0
23.4	2224	2007	0	0	0	0	1	0	2	1470	524	5	1	0	0	0	0	0	0
23.6	2268	2041	0	0	1	0	0	0	9	1488	538	1	0	0	0	0	0	0	0
23.8	2266	2037	0	0	0	0	0	0	7	1543	481	2	1	0	0	0	0	0	0
24.0	2275	2048	0	0	0	0	0	0	9	1536	486	14	0	0	0	0	0	0	0
24.2	2195	1948	0	0	0	0	0	0	3	1461	468	11	1	0	0	0	0	0	0
24.4	2280	1989	0	0	0	0	0	2	10	1500	460	9	3	1	0	0	0	0	0
24.6	2119	1873	0	0	0	0	0	1	25	1376	451	15	1	1	0	0	0	0	0
24.8	2153	1848	0	0	0	0	0	1	8	1355	457	14	5	0	2	0	0	0	0
25.0	2246	1921	0	0	0	0	1	2	14	1409	465	20	7	0	1	0	0	0	0
25.2	2258	1933	0	0	0	1	0	1	20	1415	464	28	2	1	0	0	0	0	0
25.4	2186	1844	0	1	0	0	0	3	20	1366	434	18	0	1	0	0	0	0	0
25.6	2197	1841	0	0	0	0	1	1	33	1341	428	26	4	1	3	0	0	0	0
25.8	2159	1806	0	0	0	2	2	8	42	1291	417	24	10	3	0	0	0	1	0
26.0	2006	1610	0	0	0	0	3	9	35	1157	362	29	6	3	3	1	0	0	0
26.2	2098	1702	0	0	1	1	2	9	49	1193	408	20	14	3	1	0	0	0	0
26.4	2098	1690	0	0	1	1	2	11	59	1107	451	32	11	3	5	0	1	0	1
26.6	2095	1660	0	1	0	1	3	9	69	1052	440	48	19	7	5	1	0	0	0
26.8	2028	1600	0	0	1	2	2	18	71	998	412	58	17	14	1	0	1	0	1
27.0	2070	1593	0	1	2	1	9	20	122	868	485	57	11	4	1	3	0	1	0

Table 4—Continued

F606W	N_{in}	N_{out}	$\Delta F606W$																
			-0.40	-0.35	-0.30	-0.25	-0.20	-0.15	-0.10	-0.05	0.00	0.05	0.10	0.15	0.20	0.25	0.30	0.35	0.40
27.2	1985	1472	0	1	1	1	8	18	124	739	436	80	26	14	6	4	0	1	3
27.4	2144	1588	1	1	0	4	13	29	156	728	480	100	36	18	11	2	1	1	1
27.6	2228	1609	0	1	3	6	9	48	188	675	491	114	36	10	7	5	5	2	2
27.8	2266	1602	1	2	5	7	18	41	233	571	472	151	48	17	10	5	7	3	0
28.0	2148	1518	1	2	7	10	24	73	208	502	404	174	56	23	11	6	4	2	2
28.2	2223	1469	1	4	4	11	27	92	208	381	342	197	94	39	26	9	6	2	1
28.4	2199	1397	2	0	6	18	27	89	201	312	330	194	107	47	20	9	6	6	6
28.6	2091	1236	6	3	10	14	39	100	171	241	240	174	104	46	33	19	5	5	3
28.8	2207	1310	2	6	13	26	56	114	182	226	220	156	101	74	38	29	16	10	8
29.0	2238	1247	6	6	21	33	64	111	134	195	179	158	102	73	52	30	24	12	7
29.2	2273	1202	10	13	22	45	70	109	147	150	153	110	106	63	61	34	29	20	4
29.4	2184	1088	12	20	34	51	92	84	98	115	90	109	91	62	52	39	37	26	14
29.6	2184	994	15	22	33	46	62	72	105	89	103	71	60	64	48	35	26	26	11

Note. — Each bin corresponds to the difference between recovered magnitude and input magnitude. Thus, a negative value implies that those stars were recovered as being brighter than their true magnitudes.